Sapienza
Università di Roma

Experimental optimisation of CERN 750MHz proton Radio-Frequency-Quadrupole for Surface Analysis

Corso di Laurea Magistrale in Electronics Engineering

Candidate

Mariangela Marchi
ID number 1547262

Thesis Advisor

Prof. Andrea Mostacci

Co-Advisor

Dr. Hermann Pommerenke

Academic Year 2021/2022

Thesis not yet defended

Experimental optimisation of CERN 750MHz proton Radio-Frequency-Quadrupole for Surface Analysis
Master's thesis. Sapienza – University of Rome

This thesis has been typeset by LaTeX and the Sapthesis class.

Author's email: marchi.1547263@studenti.uniroma1.it

Contents

Chapter 1

Introduction

The present thesis deals with the experimental optimisation of an accelerating structure named ELISA-RFQ. All the experimental work was carried out by the author at the CERN laboratories in Geneva, Switzerland.
The branch of application is Radio-Frequency engineering applied to particle accelerators, having had the opportunity to study, perform and apply electro-magnetic characterization, analysis and RF measurement techniques on RF devices.
The work is centered around the tuning and RF measurements of a particular typology of resonant cavity, called Radio-Frequency-Quadrupole (RFQ), operating at 750 MHz.
The name of the project is ELISA-RFQ, that stands for Experimental Linac for Surface Analysis, and it is a stand-alone accelerator with a length of only one meter that provides protons for ion beam analysis of cultural heritage artwork.
The Radio-Frequency-Quadrupole is a special type of accelerator that accelerates protons or ions at low energies, and represents a crucial component of modern linear accelerator designs.
Working at high operating frequency allows for compact and economic RFQ designs, opening up a broad variety of applications in industry and in medicine. A list of possible fields of application are: fusion research, semiconductor industry, radiography, ion implantation, ion beam analysis, isotope production, chemistry, material science, radiotherapy and more [12, 31]. Since the twentieth-century particle accelerators constitute crucial high-technological structures, whose development and improvement over the years has led to important advances in science and technology. Their purpose is to accelerate charged particles to relativistic velocities (near speed of light) and at high energies using electro-magnetic fields.
In particular the RFQ are part of the category of linear accelerators, in which time-dependent electro-magnetic fields accelerate charged particles along a straight line. An RFQ accelerates hadrons, i.e. protons or ions, at low energies [12] and

they were introduced in 1969 by Kapchinsky and Teplyakov first presented the RFQ principle [22]. One of the main advantages of the RFQ over other low-energy RF accelerators is the capability to perform adiabatic bunching converting a large portion of a continuous input beam into a train of stable bunches while minimizing space-charge effects, maintaining high beam quality. The RFQ is considered a major innovation in the field of linear accelerators. In the present days, it is employed often as the first RF accelerating structure in a hadron accelerator complex, as the beam quality achieved at low energies is a fundamental contributor to the overall accelerator performance.

1.1 Thesis Outline

The present thesis is organized as follows: Chapter 2 presents the theoretic concepts useful for the understanding of the work. It is focused on the electro-magnetic basis with an emphasis on the RF scope and resonant cavities.
Chapter 3 deals with the description of the Radio-Frequency-Quadrupole, explaining its functioning principles and field. Furthermore a section of the chapter is focused on the description of the specific geometric configuration used for this work, the four-vane RFQ. At the end a brief overview of the general design choices and specifications of the ELISA-RFQ is reported.
Chapter 4 constitutes the main and most important part of the thesis. It collects the majority of the experimental work carried-out on the physical structure. The low-power RF measurements performed on the ELISA-RFQ are presented. A large portion of this chapter is dedicated to the RFQ tuning, where frequency and field distribution were corrected by means of repeated bead-pull measurements and adjustment of movable slug tuners.
Chapter 5 covers the study developed for the input power coupler of the ELISA-RFQ accelerator. On the basis of the coupler design belonging to PIXE-RFQ [3, 4], it was decided to bring a change in the material, specifically a ceramic one, of the RF window of the coaxial coupler. Electro-magnetic simulations were performed in order to deliver geometric proposals of the coupler internal structure, taking into account the ceramic material change and RF performance requirements.

Chapter 2

RF cavities foundations

In accelerators, appropriate fields are often obtained using specially designed Radio-Frequency (RF) cavities. A RF cavity is a piece of conductor enclosing an empty volume, generally vacuum.
They can be defined as metallic chambers that can sustain an infinite number of resonant electromagnetic modes. The shape of the RF cavities is selected in such a way thar a particular mode can transfer efficiently its energy to a charged particle. In the presence of an electric or magnetic field, a charged particle is subjected to the Lorentz force, expressed in the following equation:

$$\vec{F} = q(\vec{E} + \vec{v} \times \vec{B}) \tag{2.1}$$

where $\vec{E}$ is the electric field strength, $\vec{B}$ is the magnetic flux density, q is the particle charge and $\vec{v}$ is its velocity. The electric field component alone is capable of transferring energy to the particle in the direction of its propagation, whereas the magnetic field has the effect of deflecting the trajectory of moving particles. For a charged particle to continuously gain energy in an oscillatory electromagnetic field and be efficiently accelerated, some conditions must be satisfied.
Firstly, there must be a component of the electric field which acts in the direction of the particle's motion, the so-called longitudinal dimension. Secondly, the magnetic field has to be null along the particle trajectory. Moreover, the particle must remain synchronous with the field, requiring that its velocity is equal to the velocity at which the crest of the wave travels.
This chapter aims to provide the reader with an overall explanation of concepts that form the basis necessary for understanding the work done for the present thesis. The theoretical foundations are based on explanations given in the textbook [20, 21].

2.1 Electro-Magnetic theory

2.1.1 Maxwell's equations

Electric and magnetic phenomena are classically described by Maxwell's equations, as published by Maxwell in 1873 [34].
The general form of the time-varying equations, known in their differential form as:

$$\nabla \times \vec{E} = -\frac{\partial \vec{B}}{\partial t} \tag{2.2}$$

$$\nabla \times \vec{H} = \vec{J} + \frac{\partial \vec{D}}{\partial t} \tag{2.3}$$

$$\nabla \cdot \vec{D} = \rho \tag{2.4}$$

$$\nabla \cdot \vec{B} = 0 \tag{2.5}$$

The Nabla (∇) operator expresses the curl and divergence of the vector fields which are real functions of spatial coordinates x, y, z, and the time variable t. $\vec{H}$ and $\vec{E}$ are the magnetic and electric field strengths, respectively. $\vec{B}$ and $\vec{D}$ are the corresponding flux densities, ρ and $\vec{J}$ the electric charge and electric current densities.
Another advantageous way to express the Maxwell's equations is their integral representation. By making use of the Gauss' and Stokes' theorems [20] the following equations are obtained

$$\oint_{\partial S} \vec{H} dS = \iint_S (\frac{\partial \vec{D}}{\partial t} + \vec{J}) dS \tag{2.6}$$

$$-\oint_{\partial S} \vec{E} dS = \iint_S \frac{\partial \vec{B}}{\partial t} dS \tag{2.7}$$

$$\oiint_{\partial V} \vec{D} dS = \iiint_V \rho dV \tag{2.8}$$

$$\oiint_{\partial V} \vec{B} dS = 0 \tag{2.9}$$

Taking into account the properties of matter, the electric and magnetic field strengths are related to their corresponding flux densities as:

$$\vec{D} = \epsilon_0 \epsilon_r \vec{E} \tag{2.10}$$

$$\vec{B} = \mu_0 \mu_r \vec{H} \tag{2.11}$$

Where ϵ_r and μ_r are the relative permittivity and permeability respectively. In a homogeneous, isotropic medium they are scalar quantities but, in the real instances, both generally have a spatial dependence, and take the tensor form for anisotropic materials. The zero-indexed quantities refer to the permeability and permittivity of vacuum, respectively. The electric current density consists of three contributions: an impressed current density related to external sources, a convective current density representing free moving charges, and an Ohmic current density proportional to the material conductivity σ. The latter constitutes the only relevant contribution for the work of this thesis and it is expressed as:

$$\vec{J} = \sigma\vec{E} \tag{2.12}$$

Assuming to be in the free space, in condition of harmonic time-dependence in the form of $e^{j\omega t}$ the 2.2, 2.5 become:

$$-\nabla\times\vec{E} = j\omega\mu_0\vec{H} \tag{2.13}$$

$$\nabla\times\vec{H} = j\omega\epsilon_0\vec{E} \tag{2.14}$$

$$\nabla\cdot\vec{E} = 0 \tag{2.15}$$

$$\nabla\cdot\vec{H} = 0 \tag{2.16}$$

where $\omega = 2\pi f$ is the angular frequency, and f is the regular frequency. By combining the first two equations in order to discard either $\vec{E}$ or $\vec{H}$, and incorporating the last two, the Helmholtz equations are derived:

$$(\nabla^2 + k^2)\vec{E} = 0 \tag{2.17}$$

$$(\nabla^2 + k^2)\vec{H} = 0 \tag{2.18}$$

∇^2 is the Laplacian operator and $k = \frac{2\pi}{\lambda}$ is the wavenumber. Both the equations describe electro-magnetic waves at a certain angular frequency $\omega = kc$, where $c = \frac{1}{\sqrt{\epsilon_0\mu_0}}$ is the speed of light in vacuum. If the frequency is slow and, as a consequence, the wavelength of the electro-magnetic waves is large with respect to the geometric dimensions, the quasi-static approximation can be applied. In this case the electric field becomes curl-free and can be described by means of the gradient of an electro-static potential:

$$\vec{E} = -\nabla U cos(\omega t + \phi) \tag{2.19}$$

where the potential U statisfies the Laplace's equation:

$$\nabla^2 U = 0 \tag{2.20}$$

where ϕ is the phase of the electric field oscillation.

Electro-magnetic waves propagating in free space can be described as plane waves, a single one or a superposition of many, with both the electric and magnetic field vectors perpendicular to the direction of propagation, belonging to the so-called

transverse electro-magnetic (TEM) type [21]. Considering guided electro-magnetic waves, as it happens in a resonant cavity, the solutions of Maxwell's equations, with the imposition of the boundary conditions on the conductor, allow the existence of electro-magnetic field configurations in the cavity, defined as resonant modes.
In the following section the behaviour of electro-magnetic fields inside a resonant cavity is described, as well as, important characteristics related to the general functioning of RF cavities.

2.1.2 Electro-magnetic Fields in Resonant Cavities

Resonant cavities contain electro-magnetic fields inside a volume bounded by conducting walls, so that standing or traveling waves can be established. On a boundary of infinite conductance, known as Perfect Electric Conductor (PEC), the components different from zero are the normal-electric component and the tangential-magnetic one, with respect to the conductor surface. Formally:

$$\widehat{n} \times \vec{E} = 0 \tag{2.21}$$

$$\widehat{n} \cdot \vec{H} = 0 \tag{2.22}$$

where $\widehat{n}$ is the unit vector normal to the surface of the conductor. In a similar formal way a Perfect Magnetic Conductor (PMC) is defined, where the two components are exchanged:

$$\widehat{n} \times \vec{H} = 0 \tag{2.23}$$

$$\widehat{n} \cdot \vec{E} = 0 \tag{2.24}$$

In practice no materials are either PEC or PMC. They are ideal concepts, useful in the simulation of electro-magnetic fields with the PMC boundaries being used as simmetry planes, when the field obeys Eq. 2.23, in order to simplify the field calculations and save simulation time.
Imposing the boundary conditions on the Eq. 2.17,2.18 leads to the eigenvalue problem and the electro-magnetic fields which fulfill it are denoted as the eigenmodes of the cavity, which are mutually orthogonal in the power loss structures. Their discrete eigenfrequencies $\omega_n = ck_n$ are derived from the eigenvalue k_n^2.

2.1.3 Power loss and Coupling

The energy stored in the electro-magnetic field inside the RF cavities decreases since the RF resonators are subject to power loss. Losses are of different types: dielectric, magnetic, surface losses, external losses and beam loading. For this work only the surface and external losses are of relevant importance. The Ohmic surface resistance generates a surface power loss, expressed as:

$$P_0 = \iint_S p_s dS \tag{2.25}$$

where $p_s = \frac{1}{2}\Re(Z_s)H_t^2$ is the power loss density and $Z_s$is the frequency-dependent surface impedance, defined as:

$$Z_s(\omega) = (1-j)\sqrt{\frac{\omega\mu_0}{2\sigma}} \tag{2.26}$$

Referring to a specific eigenmode, the power loss is commonly quantified through the unloaded quality factor,

$$Q_0 = \frac{\omega_0 W_0}{P_0} \tag{2.27}$$

which is a measure of the electro-magnetic energy lost per oscillation period normalized to the total energy stored in the electro-magnetic field of the eigenmode. W_0 is defined as

$$W_0 = \frac{\epsilon_0}{2}\iiint_V \vec{E}\cdot\vec{E}^* dV = \frac{\mu_0}{2}\iiint_V \vec{H}\cdot\vec{H}^* dV \tag{2.28}$$

In order to compensate the power loss occurring in the RF resonator, one or more RF input power couplers are needed to supply the required power to the cavity. The external quality factor $\mathrm{Q_{ex}}$ takes into account of the externally supplied power to the cavity,

$$Q_{\mathrm{ex}} = \frac{\omega_0 W_0}{P_{\mathrm{ex}}} \tag{2.29}$$

indicated here with $\mathrm{P_{ex}}$. Surface and external losses (and in the most general case, all the power loss contributions) are combined in the loaded quality factor $\mathrm{Q_l}$, for which the following relation holds:

$$\frac{1}{Q_\mathrm{l}} = \frac{1}{Q_0} + \frac{1}{Q_{\mathrm{ex}}} \tag{2.30}$$

In Figure 2.1 is reported the equivalent model of an RF resonator with a single input power coupler [12]. The cavity is modeled as an RLC circuit, where the shunt resistance R represents the surface losses, the capacitance C is associated to the electric field, while the inductance L identifies the magnetic field. In the specific case of the RFQ, the capacitance is given by the four electrodes forming a quadrupole channel. The transformer is associated to the coupler characterized by the coupling strength β_c (in the figure represented by the transformer ratio 1:n), which is connected to a waveguide of characteristic impedance $\mathrm{Z_0}$ (usually of the value of 50 or 75) and to an RF source matched to the waveguide. The present equivalent model is composed of lumped circuit elements and the unloaded quality factor can be expressed, with regard to them, as $Q_0 = \omega_0 RC$, where $\omega_0 = \frac{1}{\sqrt{LC}}$ is

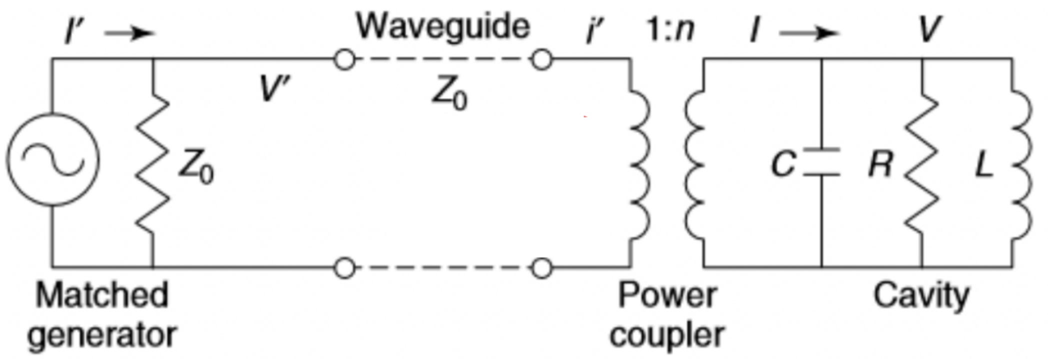

Figure 2.1. Equivalent RLC circuit of an RFQ cavity connected to a matched RF generator through waveguide and power coupler. The coupler is modeled as a transformer with a coupling strength β_c. Courtesy of Multidisciplinary Lab. Elettronica 2, "Sapienza" University of Rome.

the resonance frequency.
The coupling strength is defined as the ratio between the power P_{ex} transmitted through the coupler to the power P_0 lost on the interior cavity walls:

$$\beta_c = \frac{P_{ex}}{P_0} = \frac{Q_0}{Q_{ex}} \tag{2.31}$$

Depending on the value assumed by the coupling strength, three different coupling cases are obtained. For $\beta_c < 1$ there is the case of under-coupling, while for $\beta_c > 1$ the case is of over-coupling. The critical coupling, meaning the equality between the power lost and the one supplied to the cavity, is achieved when $\beta_c = 1$.
Considering not only the coupling strength itself, but also an offset $\Delta\omega$ between the natural resonance frequency of the cavity ω_0 and the RF source frequency, the reflection coefficient $\Gamma = S_{11}$ is given by

$$\Gamma = \frac{Z_{in}' - Z_0}{Z_{in}' + Z_0} = \frac{\beta_c - 1 - 2jQ_0\Delta\omega/\omega_0}{\beta_c + 1 + 2jQ_0\Delta\omega/\omega_0} \tag{2.32}$$

where $Z_{in}' = \beta_c Z_{in}$ is the cavity input impedance, with

$$Z_{in} = \frac{R}{1 + 2jQ_0\Delta\omega/\omega_0} \tag{2.33}$$

The reflection becomes zero only for the case of critical coupling and $\Delta\omega = 0$. The amount of surface power loss P_0 is proportional to ${V_0}^2$, that is the squared cavity voltage, which is determined by beam dynamics constraints and specifications.

2.1.4 Slater's Perturbation Theorem

The resonance frequency of an RF cavity changes when its geometry is perturbed, for instance via the displacement of cavity walls caused by heat-induced deformation, or the introduction of a perturbing object. For adiabatic changes, the change in frequency $\Delta\omega$ is proportional to the change in energy. This fact is quantified by Slater's cavity perturbation theorem [?]:

$$\frac{\Delta\omega}{\omega_0} = \frac{\iiint_{\Delta V}(\mu_0 H^2 - \epsilon_0 E^2)dV}{\iiint_V(\mu_0 H^2 + \epsilon_0 E^2)dV'} \tag{2.34}$$

where ΔV denotes the small volume that is removed from the cavity. E and H are the amplitudes of the unperturbed electric and magnetic fields, respectively, at the location of ΔV. Slater's theorem states that the frequency increases if a volume containing a strong magnetic field is removed from the cavity, and decreases if the volume contains a strong electric field. With $\omega_0^2 = \frac{1}{LC}$, removing the volume corresponds to lowering the inductance and increasing the capacitance [1]. The perturbation theorem provides the foundation of the RF field measurements [?], as well as frequency and field adjustments by means of tuners introduced into the RFQ cavity, that are later discussed in 4.

Chapter 3

The Radio-Frequency-Quadrupole Linac

The Radio-Frequency-Quadrupole (RFQ) is a low-velocity, high-current linear accelerator which focuses, bunches and accelerates a continuous beam of charged particles by means of an RF electric field. The RFQ is characterized by the ability to provide high efficiency and high emittance, preparing efficiently a low-energy hadron or ion beam to be accelerated in a conventional Drift Tube Linac (DTL). The history of the RFQ accelerator began in 1970 from the idea of Kapchinskij and Teplyakov [22]. Nowadays RFQs are broadly used in order to realize efficient, compact and economic injectors for linacs and cyclotrons, stand-alone accelerators as well as post-acceleration structures.
In this chapter the RFQ principles of operation are explained and an analytical description of the electro-magnetic field occurring inside this kind of RF structure is provided.
Then, a section is dedicated to the four-vane RFQ, which constitutes the geometric RFQ configuration of interest for the present work.
The chapter is completed by an overview of the design specifications, choices and description of the physical project object of this thesis, ELISA-RFQ.

3.1 Principles of operation of the RFQ

A RFQ consists in a cavity loaded with four electrodes which are positioned in parallel to the beam axis direction as shown in Figure 3.1.

A time-alternating voltage $\pm\frac{V_0}{2\cos\omega t}$ is applied to the four electrodes such that

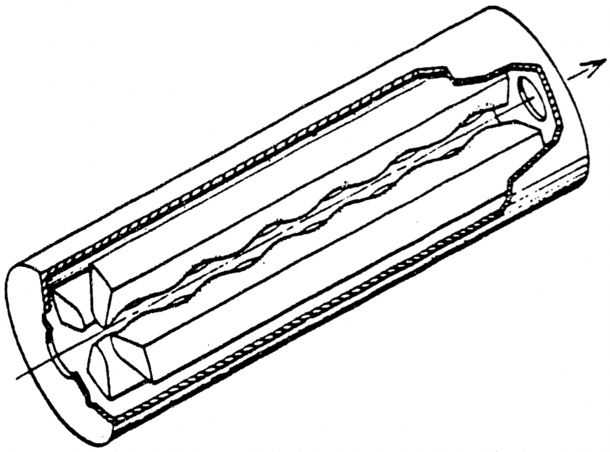

Figure 3.1. Sketch of a four-vane RFQ cavity - Courtesy T.Wangler

the two adjacent electrodes present opposite polarity, whilst the two opposite ones show the same voltage polarity. V_0 is the peak potential difference between two adjacent electrodes and is denoted as inter-electrode voltage (inter-vane voltage in the case of the present thesis). Such a configuration produces a quadrupole electric field, causing the cavity to resonate in the TE_{210} mode, and, consequently, electric transverse focusing and defocusing forces which operate alternately in time on the beam.
Acceleration is produced by adding a perturbation to the RF quadrupole structure in order to generate longitudinal fields which bunch and accelerate the beam. The added geometric perturbation is a periodic modulation of the electrodes in the longitudinal direction.
Moreover the RFQs use the adiabatic bunching which splits the beam into bunches at the operating frequency while keeping the minimum loss and the minimum longitudinal emittance of the beam.

3.1.1 Focus and Bunching

Given the structure characterizing the RFQ it is appropriate to describe in greater detail its operations on the beam starting from its strong focusing effect. The transportation of the beam is realized applying the principle of alternating-gradient focusing, based on the idea of incorporating a sequence of focusing and defocusing lenses. Quadrupoles are lens that provide strong focus in the transverse plane, whereas defocus on the other. It follows that a sequence of quadrupoles of alternating polarity will focus in both planes.
The focusing period length is equal to $\beta\lambda$, where β is the velocity of the particle

and λ is the RF-wavelength. On the other hand the focusing strength, reported in Eq. 3.6 is independent from the charged particle velocity and the focusing results uniform along the entire RFQ channel.
Another important characteristic of the RFQ cavity is its ability to capture and bunch the beam with a high efficiency. The bunching operation is possible by slowly decreasing the longitudinal electrical field along the axis of the RFQ, including short cells at the beginning of the structure which gradually elongate towards the end of it. This process could require a considerable number of unit cells making it not economically convenient in specific cases.

3.1.2 Acceleration

Acceleration in an RFQ is achieved by periodically modulating the electrodes' surface in the longitudinal direction as shown in Figure 3.2. The periodic longitudinal

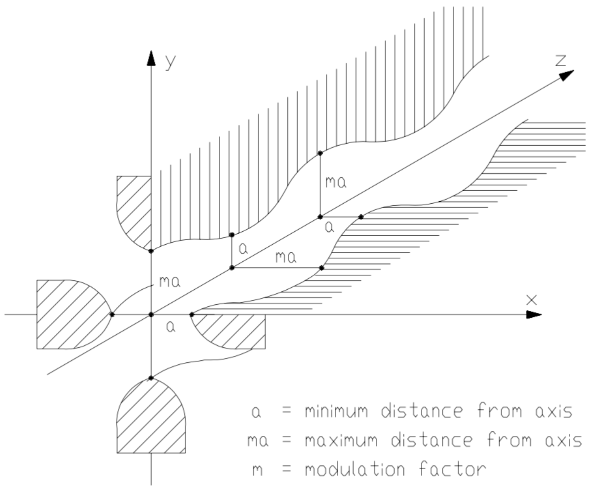

Figure 3.2. Longitudinal modulation of the vane profiles.

modulation, which is 180 degrees out of phase in the top/bottom electrodes with respect to the left/right pair, deforms the pattern of the pure TE mode by creating a longitudinal component proportional to the depth of the modulation. The synchronism between the increasing velocity of the particle and the longitudinal component can be controlled with the wavelength of the modulation. The ripples of the modulated electrodes' profile has only a small effect on the transverse focusing field.

3.2 Field in a RFQ

The field between the electrodes is commonly described by means of a multipole potential function, where the electric potential is expanded in terms of longitudinal and azimuthal harmonics. In a RFQ the electric and magnetic fields are separated in space, with the magnetic field vanishing towards the beam. In the area between the four electrodes the electric field, in the proximity of the beam, can be described by a quasi-static approximation 2.20. The potential in this area (between the vane tips,for a four-vane RFQ) can be expanded as a Fourier-Bessel series.
Assuming that a voltage of $\pm\frac{V_0}{2}$ is applied in an alternative manner to the RFQ electrodes:

$$\frac{U(r,\theta,z)}{V_0/2}=\sum_{m=1}^{\infty}A_{0m}(\frac{r}{r_0})^2mcos(2m\theta)+\sum_{m=0}^{\infty}\sum_{n=1}^{\infty}A_{nm}I_{2m}(nkr)cos(2m\theta)cos(nkz) \tag{3.1}$$

Here, n and m are the longitudinal and azimuthal indices, while the function I_n stands for the modified Bessel function of the first kind and order n. Moreover, r_0 is the mid-cell aperture, $k=\pi/L$ is the spatial wavenumber, and A_{nm} are the multipole expansion coefficients. To simplify the general potential function it can be considered, to a good approximation, the two first terms that characterize the potential near the axis, deriving the so-called two-term potential function:

$$\frac{U(r,\theta,z)}{V_0/2}=(\frac{r}{r_0})^2cos(2\theta)+AI_0(kr)cos(kz) \tag{3.2}$$

where $A_{01}=1$ and A_{10} is referred as A and represents the two-term potential acceleration parameter. Figure 3.2 shows a sketch of the modulated vane profile. The distance between the beam axis and the vane surface is comprised between the values a and ma, where $m>1$ is the modulation factor. The unit cell length is $L=\frac{\beta\lambda}{2}$. In order to establish a longitudinal field, the even and odd vanes have different distances from the axis. Indeed, the even vanes are spaced a distance a from the axis and the odd vanes a distance ma. Observing the profile along the longitudinal direction, the even-odd distances are reversed, cell by cell, so that an axial accelerating field is generated which depends on the modulation factor m.
By applying the boundary conditions at the beginning and at the end of the unit cell for even and odd vanes, the two-term potential function gives:

$$(\frac{a}{r_0})^2+AI_0(ka)=1,(\frac{ma}{r_0})^2-AI_0(mka)=1 \tag{3.3}$$

which give

$$A=\frac{m^2-1}{m^2I_0(ka)+I_0(mka)} \tag{3.4}$$

$$(\frac{a}{r_0})^2=1-AI_0(ka) \tag{3.5}$$

The last quantity is defined as the quadrupole focusing efficiency, $\chi = 1 - AI_0(ka)$. The focusing strength is identified as:

$$B = \chi \frac{qeV}{mc^2} \frac{\lambda^2}{a^2} \tag{3.6}$$

It can be seen that if A increases, which is related to an upgrade of the longitudinal electric field strength, the focusing efficiency decreases. Generally, the transverse electric field acting on the beam is much higher than its longitudinal component, so the RFQ has strong focusing but limited acceleration capabilities.

3.3 Four-vane RFQ Cavity

One of the two possible main configurations for a RFQ cavity is the so-called four-vane structure, which is the one considered for the RFQ of the present thesis. Pictures of the four-vane cavity are shown in Figure 3.5.
The four-vane RFQ is mainly employed in the high-frequency range,with a frequency higher than 200 MHz,for the acceleration of protons or light ions. The configuration used for the low-frequency applications is the four-rod RFQ [23].
With the four electrodes arranged in the shown configuration, which resembles a cloverleaf geometry, it is possible to achieve the TE_{210} operating mode. The vanes are resonators with the capacitance concentrated between the vane tips and the inductance present in the inter-vane space. Figure 3.3 shows the equivalent circuit of the ideal four-vane cloverleaf geometry. In the four-vane cavity two types of

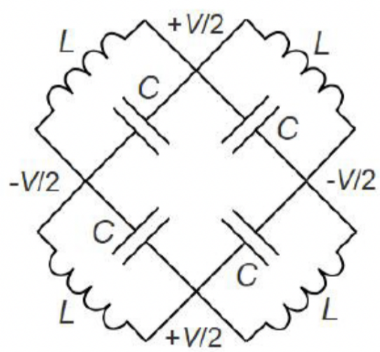

Figure 3.3. Equivalent circuit of the ideal four-vane RFQ.

eigenmodes are distinguished by their transverse field pattern: quadrupole modes and dipole modes, the latter in two different polarizations.
Quadrupole modes and dipole modes are denoted as TE_{21n} and TE_{11n}, respectively, where TE indicates that the field patterns are transverse-electric and the first and

second subscripts identify the number of azimuthal and radial periods, respectively, whereas the last subscript n denotes the number of longitudinal half-wavelengths. The operating mode of the RFQ is the TE_{210} quadrupole mode. This kind of field distribution can't exist in a cylindrical cavity with short-circuited, almost-PEC metallic terminations [12], so particular and dedicated designs are needed.
The four-vane RFQ is characterized by spatial separation of electrical and magnetic fields, as it can be seen in Figure 3.4 that shows a cross-section of the cavity with transverse field patterns: the electric fields at the vane tips, represented by lines, while the magnetic fields flow between the four quadrants. The spatial distribution of the electro-magnetic field inside this topology is described by the lumped circuit model in Figure [**?**]. The capacitance at the vane tips models the capacitive load provided by the electric field, which is strong in those areas. The inductances model the magnetic field inside the cavity volume. The capacitances form with the shunt inductances resonant circuit that are tuned at the frequency of the TE_{210} operating quadrupole mode.
The resonant angular frequency, in relation of the equivalent circuit model, is written as

$$\omega_0 = \frac{1}{\sqrt{LC}}. \tag{3.7}$$

For the quadrupole and dipole modes the shunt inductance has the same value. The dipole modes resent of the capacitance between the adjacent vanes and also of the capacitance load present between opposite vanes. For this reason the dipole cutoff frequency is always lower than the quadrupole cutoff frequency.

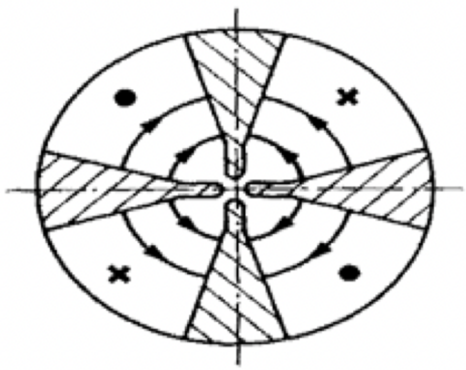

Figure 3.4. Cross-section of a four-vane cavity with spatial distribution of transverse electric and magnetic fields.

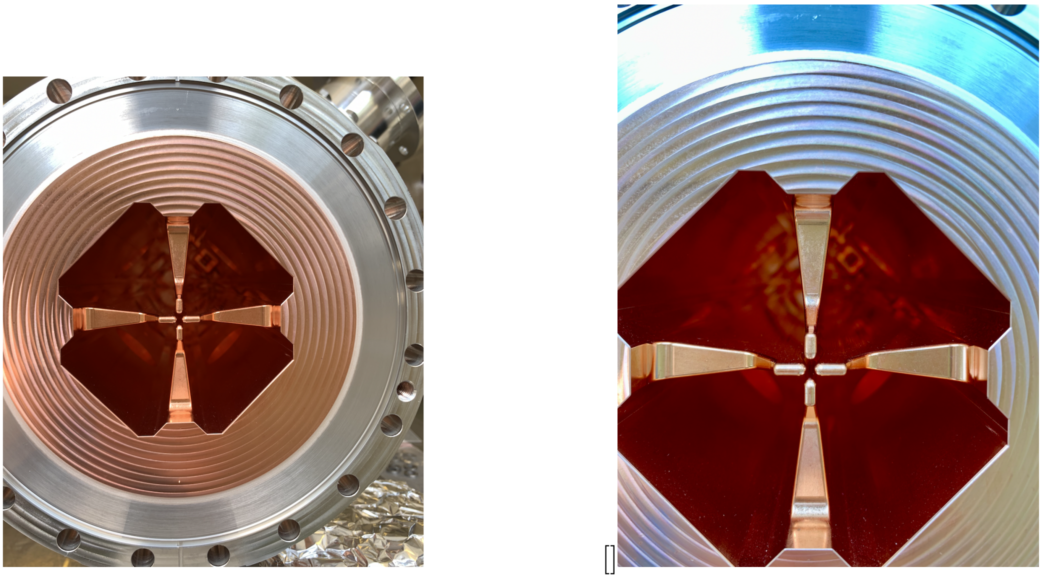

Figure 3.5. Photographs of the four-vane ELISA-RFQ operating at 750 MHz.

3.4 Overview of the ELISA-RFQ Accelerator

The aim of this section is to provide information, design specifications and parameters of the ELISA-RFQ structure. ELISA-RFQ is a compact stand-alone machine, constructed at CERN, operating at 750 MHz. Its design is the same of the previous project PIXE-RFQ [1, 2, 3, 4], sharing with it the context of the MACHINA project (Movable Accelerator for Cultural Heritage In situ Non-destructive Analysis [32, 33]), a collaboration between CERN and Istituto Nazionale di Fisica Nucleare (INFN), Florence, Italy.
The ELISA-RFQ is a transportable system capable of performing proton-induced X-ray emission analysis of materials and surfaces. One of its main characteristic is the compactness, which requires low power consumption.
It consists of almost two half-meter long modules as well as two end plates that were each vacuum-brazed individually. It features a total of 24 ports with a diameter of 36 mm, which found the support for sixteen tuners, seven vacuum pumping ports, and a single input power coupler. Eight additional smaller ports were added for RF field pick-up antennas for diagnostic purposes.
The design from an RF point of view was dictated by the optimization of the two-dimensional cross section of the RFQ, taking into account the desired operational frequency and minimum power loss as well as geometric limits regarding the vane shape and thickness. The RFQ key parameters are listed in Table 3.1.

The designed vane tip geometry was given by specific beam dynamics studies. Also the constant nominal inter-vane voltage $V_0 = 35\,\text{kV}$, which was chosen in order

Table 3.1. Key parameters of the ELISA-RFQ.

Species	Proton	(H^+)
Input energy	20	keV
Output energy	2	MeV
RF frequency	749.480	MHz
Inter-vane voltage	35	kV
RFQ length	1072.938	mm
Vane tip transverse radius	1.439	mm
Mid-cell aperture	1.439	mm
Minimum aperture	0.706	mm
Final synchronous phase	−15	deg
Output beam diameter	0.5	mm
Beam transmission	30	%
Unloaded quality factor (Q_0)	6000	
Peak RF power loss	65	kW

to permit low consumption, comes from the results of beam dynamics studies [2, 6]. Indeed the choice of the inter-vane voltage is crucial in the computation of the total RF power P_0 dissipated on surface losses. In the present design the total power loss in the RFQ was obtained making use of a segmented model as follows

$$P_0 = \omega_0 \frac{V_0^2}{2} \sum_n \frac{1}{Q_{\mathrm{o,n}}} \int_{z0,n}^{z1,n} C(z)dz \tag{3.8}$$

where C is the quadrupole capacitance, which varies along the cavity because of the vane modulation, computed considering discrete segments along the longitudinal direction. The same happens to the unloaded Q factor, whose values were obtained by individual simulation of each cell. All the contributions were summed up, thus giving the total dissipated power.

Chapter 4

RF Measurements and Tuning of the RFQ

In this chapter the description and the implementation procedure of the low-power RF measurements as well as the tuning of field and frequency of ELISA-RFQ are reported. As mentioned before, the stand-alone accelerator consists of two four-vane RFQs, each of which is subject to manufacturing imperfections, defects and misalignments that generate perturbations affecting the field distributions inside the cavity. A disruption of the ideal quadrupole field of the TE_{210} operating mode would be the main consequence of these perturbations, and such an effect must be avoided by means of bead-pull measurements and movable piston tuners.

4.1 Premises

Before presenting in detail the measurement procedures carried out and their results, as well as the tuning process, it is necessary to provide the reader with relevant and contextual information. Firstly the list of the utilized devices and tooling is reported. After that a fundamental step that has been considered since the first measurements on the single modules is described, dealing with the correction on frequency measurements affected by ambient parameters, such as uncontrolled temperature and air inside the RFQ. Lastly the principle of Bead-Pull measurements and tuning goals are reported.

4.1.1 Measurement Equipment

The experimental instruments and tooling considered for most of the measurements, above all the RF low-level ones on the RFQ, are the same as the ones utilized for the PIXE-RFQ [4]. The equipment components are listed below:

- Keysight E5061B, 100 kHz to 3 GHz Vector Network Analyzer (VNA) [?];
- keysight 85032F Type-N 50 Ω mechanical calibration kit [?];
- Keysight 12 ft (3.7 m) rugged phase-stable RF cable with 50 Ω characteristic impedance;
- Hanna Instruments HI98509 Checktemp 1 thermometers, in order to measure RFQ temperature (0.1 K scale resolution, ±0.2 K accuracy
- Extech(R) Instruments humidity detector.

4.1.2 Frequency Correction

Before analyzing the results coming from the RF measurements, in terms of the cavity spectrum, one has to pay attention to diverse aspects which potentially influence the results obtained in a significant way. In the present case RF measurements the measured frequency was affected by two main aspects:

1. thermal expansion (or contraction) of the RFQ cavity, since its bulk temperature changes along the ambient one,
2. air electrical permittivity ϵ_r, which is different to the one of vacuum, since Bead-Pull measurements are conducted under air.

Indeed, the majority of measurements were conducted in an environment in which the temperature was not strictly controlled and the medium filling the cavity was air instead of vacuum. These conditions differ from the nominal ones considered during the manufacturing process of the RFQ modules, where the reference temperature was set equal to $20°C$ and the medium was vacuum, making the measured resonance frequency values differ from the expected ones. Regarding the temperature dependence, if the copper bulk temperature increases (decreases), the measured frequency would be smaller (larger) because of the thermal expansion (contraction) experienced by the cavity body. The relation that explains the dependence between the frequency shift and the linear strain is reported below:

$$\frac{\Delta f}{f} = -\alpha_T \Delta T = -\frac{\Delta\lambda}{\lambda} \tag{4.1}$$

where $\alpha_T = 1.6610^{-5}/K$ is the linear thermal expansion coefficient of the copper cavity and ΔT represents the difference between the measured and nominal temperature. Before deriving the formula which applies the correction to the measured frequency the second major effect is analyzed, considering that the air atoms inside the RFQ structure interact with the electromagnetic fields reducing the speed of light by a factor of $\sqrt{\epsilon_r \mu_r}$ compared to the speed of light in vacuum c [25]. At standard temperature and pressure (STP) for air it could be assumed that $\mu_r = 1$ and $\epsilon_r = 1.00058986$ [26] such that the frequency could be corrected by using the following relation:

$$f = f_{meas} \cdot \frac{\sqrt{\epsilon_r}}{1 - \alpha_T \Delta T} \tag{4.2}$$

However, also the relative permittivity of air shows a dependent behaviour on a further source of uncertainty, which proves to be the ambient humidity. In fact the relative permittivity of air can be determined from the empirical equation [27]

$$\epsilon_r = 1 + \frac{211}{T} \cdot (p_{air} + \frac{48 \cdot p_{vap}(T)}{T} \cdot RH) \cdot 10^{-6} \tag{4.3}$$

where T is the absolute temperature in K, RH is the relative humidity in %, p_{air} is the air pressure in mmHg and p_{vap} is the saturation vapor pressure of moist air in mmHg. The latter is derived from another empirical equation, the Buck equation [28, 29]:

$$p_{vap} = 4.584 \cdot exp[(18.678 - \frac{T}{234.5}) \cdot (\frac{T}{257.14 + T})] \tag{4.4}$$

where the temperature is in $°C$ here. Taking into account all these factors the exact shift frequency occurring can be determined and corrected. Figure 4.1 shows the effectiveness of the present procedure, considering two measured frequencies with different situations in terms of temperature and RH in the original form and the corrected form. The following figures depict how the resulting frequency shift change as a function of temperature for two different values of RH, as well as the relative permittivity of air.

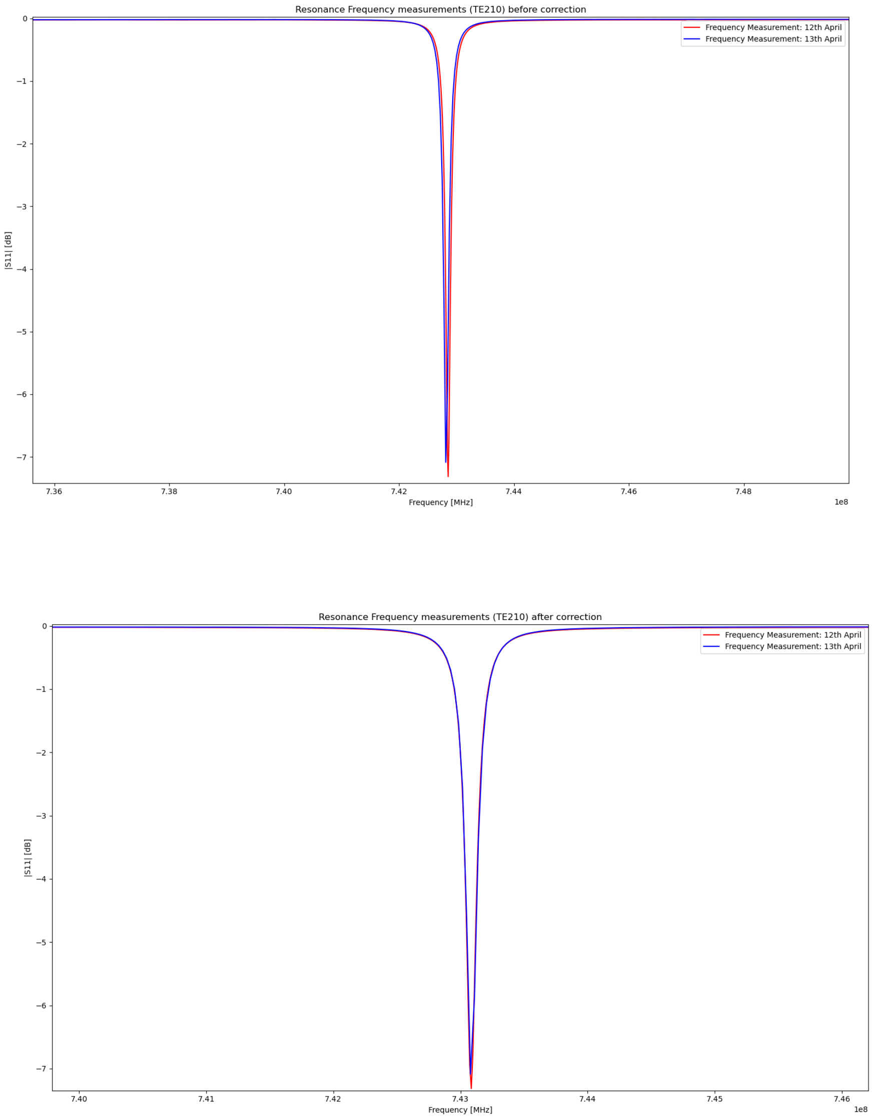

Figure 4.1. Example of application of frequency correction.

4.1.3 Bead-Pull RF System

Bead-Pull Radio Frequency measurement system represents a practical implementation of the Slater perturbation theorem (2.1.4) and it is used for measuring the RF electric and/or magnetic fields along the position in the RF cavity. To perform this kind of measurements a small metallic or dielectric bead (depending on the application) is attached to a single, thin fishing wire, which moves through each of the four quadrants of the cavity by means of a motor. A schematic representation of a Bead-Pull cavity measurement setup is shown in Figure 4.2. The bead represents

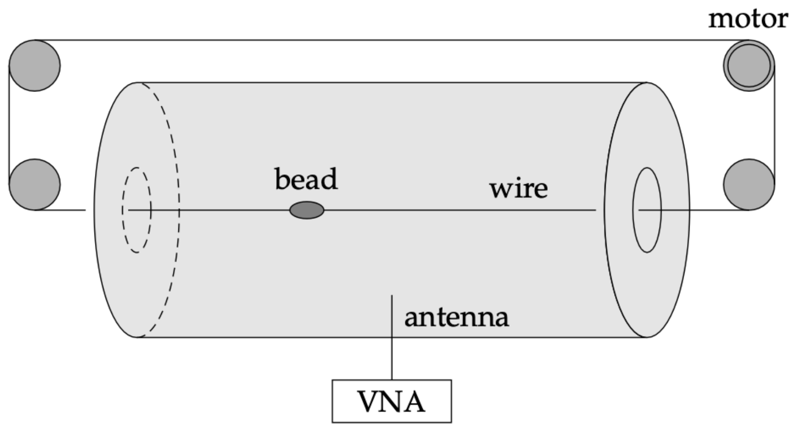

Figure 4.2. Schematic model of the bead-pull setup used to measure the field amplitude in an RF cavity.

a small volume that is subtracted from the internal volume of the cavity in each position through which the bead passes, assuming in fact the role of a perturbation, causing a shift in the resonance frequency of the cavity. The frequency shift is proportional to the combination of the squared amplitudes of the electric and magnetic fields at the location of the bead, as it is shown in the Eq. **??**. For ELISA-RFQ the same bead-pull bench, pulley system and tools as for the PIXE-RFQ and also as for the previous project HF-RFQ has been used [2, 3, 4].
An aluminum bead with a length of 7 mm and a diameter of 4 mm was threaded on a 0.3 mm fishing wire and the verse of its movement was controlled and reversed appropriately using a dedicated DPDT switch.
Given the size of the considered bead, which is not compatible with the possibility of inserting it in the region of high electric fields (i.e. between the vane tips), this was introduced and moved through the four quadrants of the RFQ, the magnetic field region of the cavity. For ELISA-RFQ, as also done for the previous project PIXE-RFQ [4], the magnetic field amplitude has been obtained starting from the measurement of the reflection scattering parameter S_{11}, since the RFQ features a single power coupler and also the use of only one antenna is sufficient for the single module measurements.
In particular, for the bead-pull measurements, it is preferable, in terms of accuracy, to measure the phase shift of S_{11} happening once the bead is introduced inside the cavity, having set the exciting wave equal to the cavity resonance frequency when the bead is out ω_0.
Figure 4.3 shows the shift of the resonance frequency and the corresponding phase shift occurring when the bead is located inside the cavity. The experienced shift in

the phase lies within the linear behaviour for small Δf.

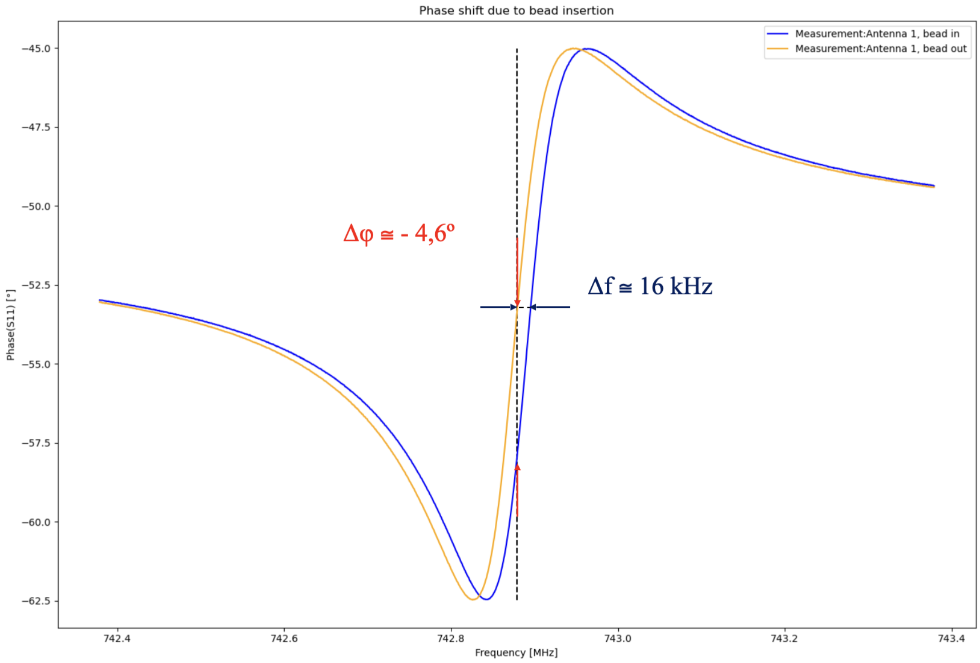

Figure 4.3. Phase and frequency shift due to bead insertion.

Since the measurement considered in the figure above was performed during the single module measurements of the first module, where a strongly under-coupled antenna has been used, the phase shift is negative. If the same measurement was taken using, for instance, the single power coupler,as it happened with the RFQ fully assembled, the phase shift would be positive. For this reason, only the magnitude of the change of the phase is of interest.
The inter-vane voltage can be determined starting from the measured magnetic field amplitude H in the four quadrants. The used relation is a consequence of Faraday's law (Eq. 2.7) and is the following:

$$V_0 = \omega\mu_0 \iint_S H_z \, dS \tag{4.5}$$

From this point, it is possible to consider that:

$$\Delta\phi \propto \Delta f \propto H^2 \propto V_0^2 \tag{4.6}$$

Starting from the measurements of the reflection coefficient phase of the four quadrants, the quadrupole and dipole components of the magnetic field amplitude have been obtained. Figure 4.4 reports all the processing steps applied on the raw measurement data :

1. raw measurement data

2. vertical alignment of the signals, done by averaging few tens of samples corresponding to the position of the bead inside the two extension tubes,so just before entering the cavity (i.e. the straight behaviour at the beginning and at the end of the field profile, in which $H \approx 0$)

3. linear interpolation , which corrects the random observable phase drift originated by the VNA itself

4. application of Savitzky-Golay filter [30], which operates data smoothing in order to reduce noise factor

5. longitudinal alignment using intersections of the rising and falling slopes with the third-maximum line which would compensate also for any systematic wire slippage between the quadrant measurements.

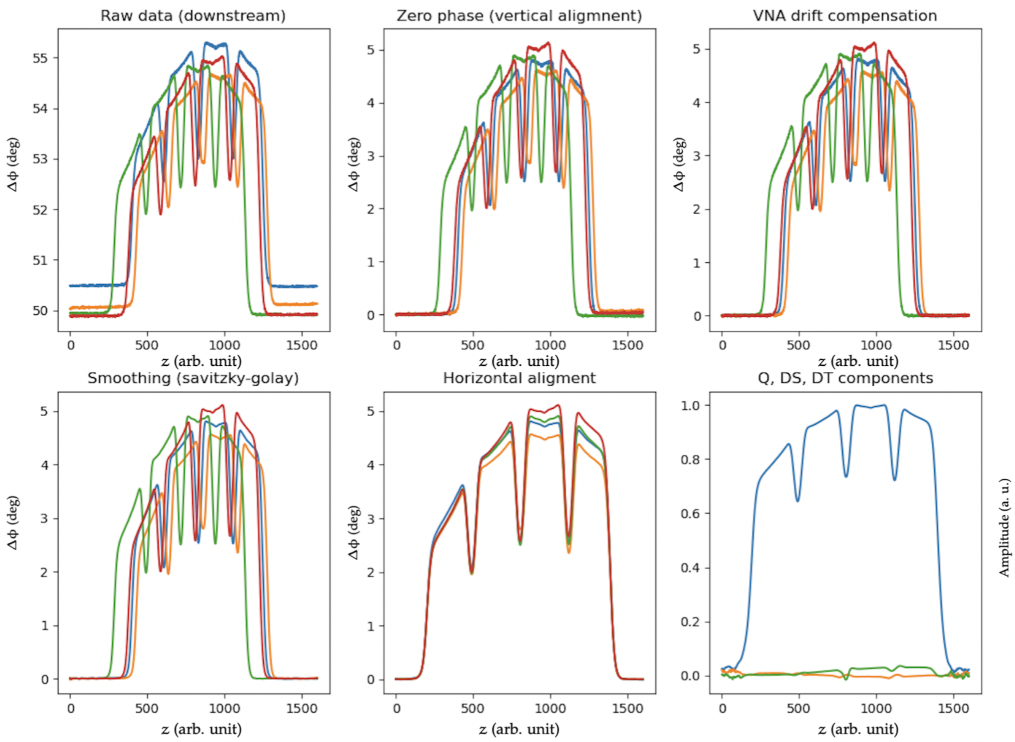

Figure 4.4. Post-processing steps applied on the Bead-Pull data obtained from the VNA reflection coefficient phase measurement.

The field profile flatness of the operating TE_{210} mode can be quantified by three field components, the quadrupole component Q and two dipole components D^S and D^T, defined in the following way [12] :

$$Q = \frac{1}{4}(a_1 - a_2 + a_3 - a_4),$$

$$D_S = \frac{1}{2}(a_1 - a_3),$$
$$D_T = \frac{1}{2}(a_2 - a_4).$$

4.1.4 Tuning goals and tooling

A change in the cavity volume or local variations in the longitudinal capacitance or inductance profiles lead to a local change of the cutoff frequency and, ultimately, of the voltage of the operating mode. The inter-vane voltage, in the present case, is designed to be equal to 35 kV and must be kept at this constant value, in order to obtain a flat magnetic field along the longitudinal dimension of the RFQ with the same magnitude in all the four quadrants. Quantitatively the aim of the tuning process is to achieve $Q = 100\%$ and $D^S = D^T = 0$ at all sampling points with an acceptable error margin of $\pm 2\%$ imposed by the beam dynamics design of the RFQ [8]. Frequency accuracy represents a less critical tuning goal, since ELISA-RFQ is a stand-alone accelerator, without RF structures attached downstream the RFQ. From this point of view, the frequency margin is set by the water temperature range of the cooling system of an RF cavity, from which it derives the sensitivity of the ELISA-RFQ resonant frequency of -13.3 kHz/K. The target value to achieve becomes 749.480 MHz under vacuum at 23 °C with an error within the range ± 60 kHz.

4.2 Validation Measurements of RFQ components

Radio-Frequency measurements of the RFQ and its auxiliaries are necessary to validate the construction quality. Both the mechanical modules which constitute the cavity were subject of such measurements, as well as the four pick-up antennas. In carrying out the work on ELISA-RFQ for the present thesis, the input power coupler used for PIXE-RFQ has been implemented, since the ceramic coupler was not available yet at the time of the RF measurements and tuning of the cavity. For this reason the coupler Head-on measurements are reported in [4].

4.2.1 Single RFQ Modules Measurements

The RFQ consists of two mechanical modules, brazed individually and then clamped together to form the full assembly. The position of the vanes were measured, with respect to the ideal beam axis, for every construction step. From the metrology data, collected after the final brazing step, the displacements were within ± 10 µm for the first module and ± 17 µm for the second one.
By means of the Bead-Pull technique presented in 4.1.3 single module measurements

were carried out. The measured resonance frequencies and longitudinal field distribution obtained for each of the two modules of the RFQ, denoted as module 1 and module 2, were compared to the simulation data (obtained using eigenmode solver of CST Microwave Studio R 2020).
From the comparison it was observed a close agreement and it was possible to deduce that no emergency measures were needed for the tuning.
In Figure 4.5 is reported a picture of the first module mounted to the RF test bench used to perform single module measurements.

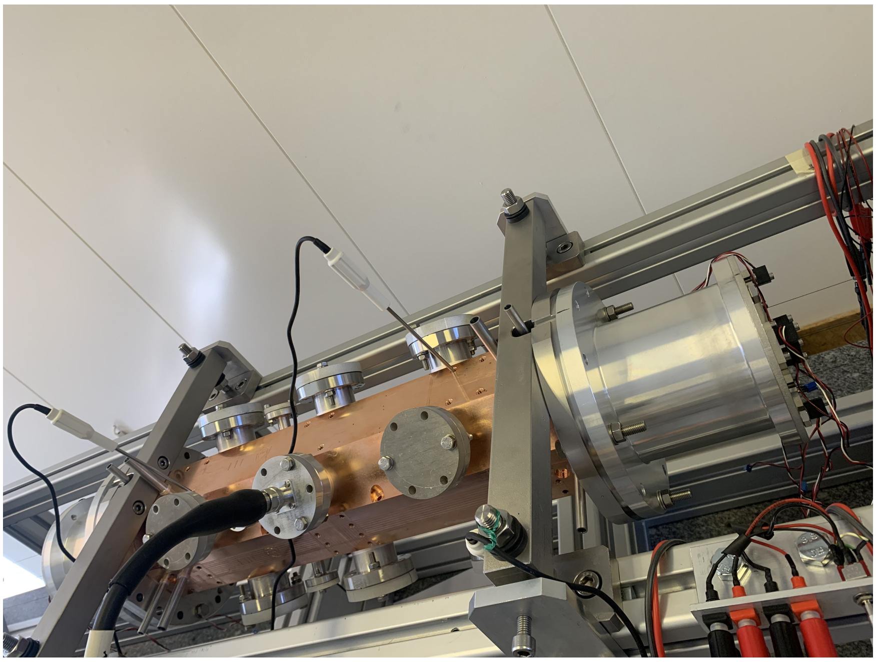

Figure 4.5. Photograph of the first module of ELISA-RFQ mounted to the RF test bench. One of the two extension tubes, temperature sensors are also visible.

All the ports present longitudinally on the four sides of the modules were closed by aluminium flange covers, whilst at the upstream and downstream ends of the modules were installed two aluminium extension tubes to guarantee the presence of well-defined boundary conditions. The length and diameter of these tubes were adjusted, by simulations [4] [8],in order to let the field decay within them and to match the frequency of the RFQ. In particular the length was chosen in such a way that the frequency became independent of it.
Before proceeding with the measurements much attention has been paid to guarantee the correct preparation of the Bead-Pull setup, including the alignment of the wire in the chosen position equal,in the azimuthal and radial directions, in all four quadrants of the RFQ. For the single module measurements a small strongly

under-coupled antenna crafted from copper was mounted to one of the ports of the modules, since the input power coupler and RF pick-up antennas were absent.For both modules the TE_{210} frequencies stand approximately $6MHz$ below the RFQ design frequency of $749.48MHz$, due to the presence of the metallic extension tubes, acting as mismatched loads on the operating mode, and the absence of auxiliaries. Figure 4.6 shows the mode spectra measurements of both the modules individually, where the first two dipole modes TE_{110} and the operating quadrupole mode TE_{210} are visible.
The observed deviations between the measured frequencies and the simulated ones for the operational quadrupole mode amount to 0.7 MHz and less than 100 kHz for module 1 and module 2, respectively. In Figure 4.7 there are the field components profiles, where the dipole components D_S and D_T slightly deviate from the ideal zero simulation value, reaching amplitudes of up to ±3 %, whereas the quadrupole component Q shows a very good agreement with the simulated profile, with a deviation of less than ±1 %.

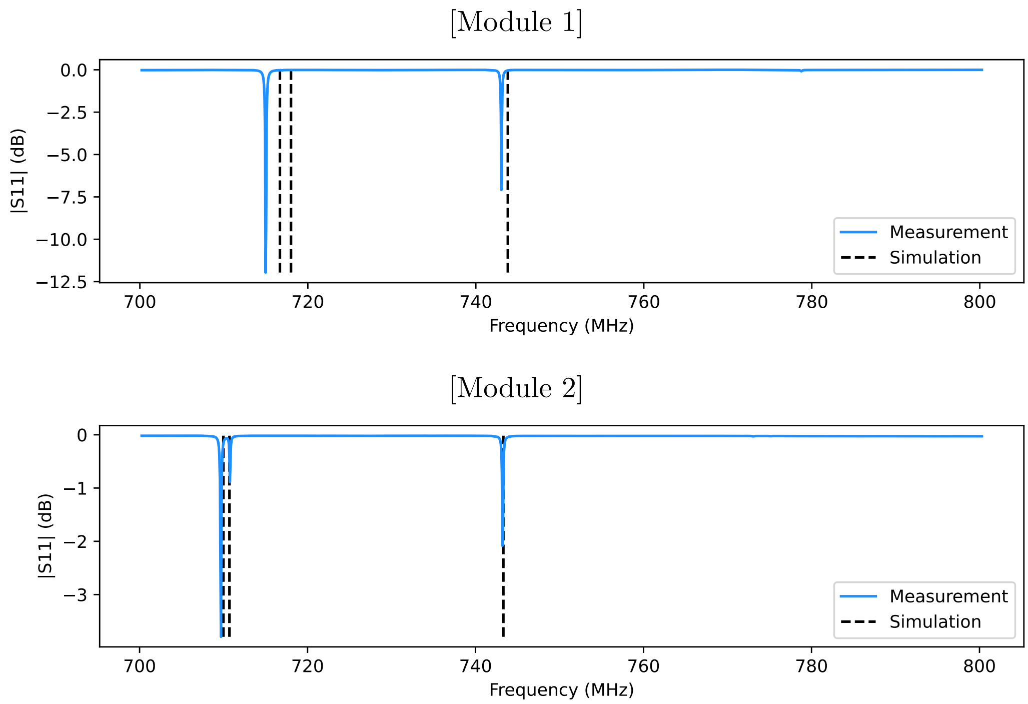

Figure 4.6. Measured reflection coefficient vs frequency for the single modules.

[Module 1]

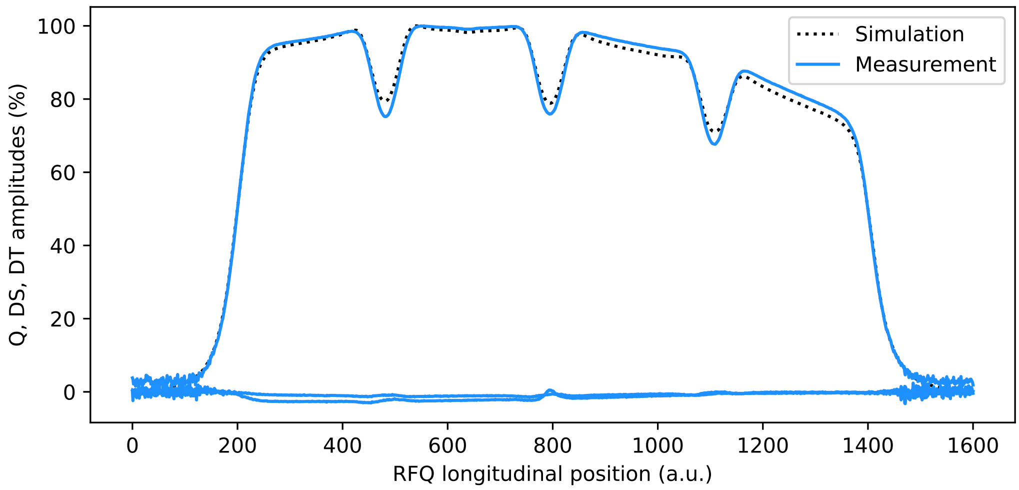

[Module 2]

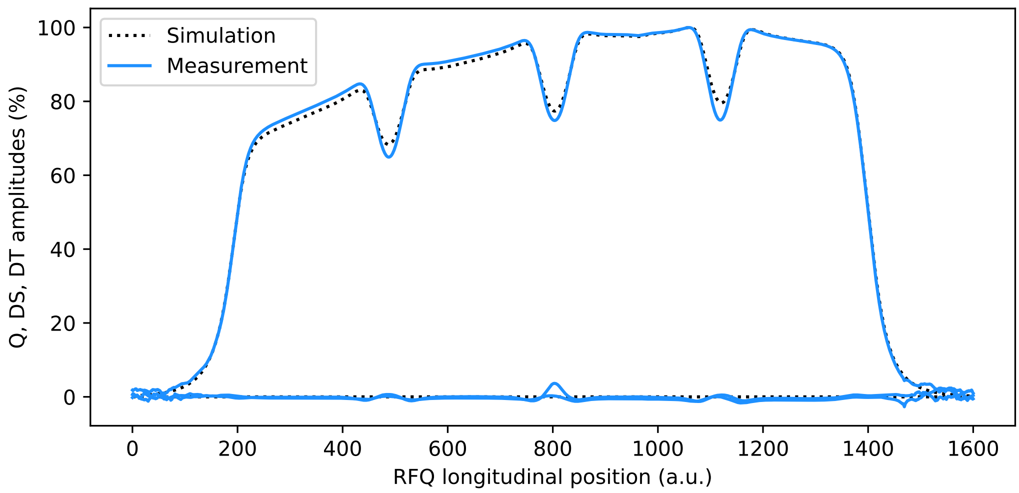

Figure 4.7. Measured quadrupole component Q and dipole components D^S, D^T of the single modules compared to the simulation.

4.2.2 Pick-up antennas head-on measurements

This section deals with measurements carried out to assess the construction quality of four pick-up antennas used as non-intercepting beam diagnostic structures, before their installation. Each pair of the four antennas was measured in a head-on configuration, where both the antennas were mounted, facing each-other, in a purpose built aluminum tube. The transmission coefficient S_{21} was measured as function of frequency for the high-transmission arrangement where the antennas are rotated around their common axis by angle $\Theta = 0\,\mathrm{deg}, 180\,\mathrm{deg}$, so that the coupling loops are closest to each-other.

Figure 4.8 reports the measured transmissions and the simulation result, showing that the deviations are acceptable, within 4 dB, since the antennas are calibrated after the installation in the RFQ.

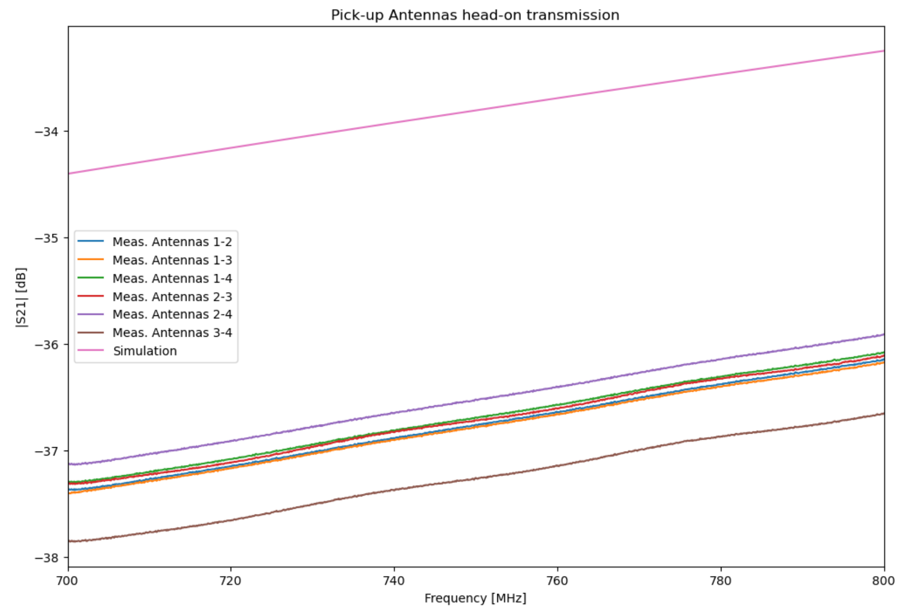

Figure 4.8. $|S_{21}|$ vs frequency between each pair of antennas with simulation result.

4.3 Tuning

After the assembly, the full RFQ was tuned by means of sixteen piston tuners. Bead-Pull measurements were performed to monitor the cavity behaviour at each step of the iterative algorithm until the final and corrective length of each tuner was found.In this section the tuning setup, algorithm and procedure steps are reported. Field and frequency values before and after the tuning process are compared and discussed.

4.3.1 Tuning Setup

The tooling used to operate the tuning process on the RFQ of the present thesis was previously used for the PIXE-RFQ [4] and originally developed for the HF-RFQ [8]. The movable copper piston tuners were mounted in the way shown in Figure 4.10, four tuners each mounted at four available positions present on each side of the cavity, for a total of sixteen of them.
The tuners were mounted in guidance tubes present on the outer surface of the port flanges so that it was possible to change carefully and purposefully their insertion inside the cavity volume, according to the results coming from the algorithm iterations.
Figure 4.9 shows a closeup of tuner tooling used for its installation. The nominal

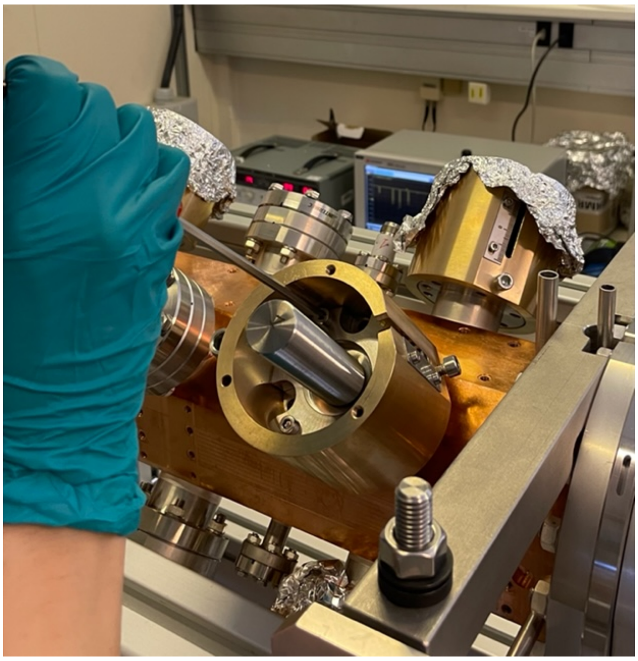

Figure 4.9. Photograph taken during the installation and fixation of one tuner inside the guidance tube.

length of the tuners correspond to having them mounted in the so-called flange-to-flange position and inserted into an ideal cavity. They were machined with an over-length of 11 mm so that it was possible to gain a mechanical tuning range of ±11 mm.
Figure 4.10 shows the full assembly of the RFQ which includes the two modules brazed together, pumping ports, the RF input power coupler, four diagnostic antennas and the two end plates.

Designations of the RFQ quadrants and tuners.

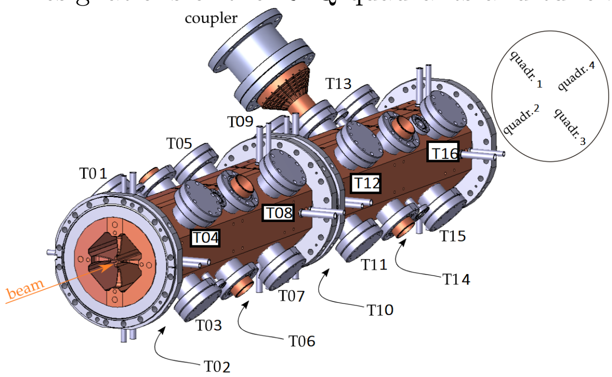

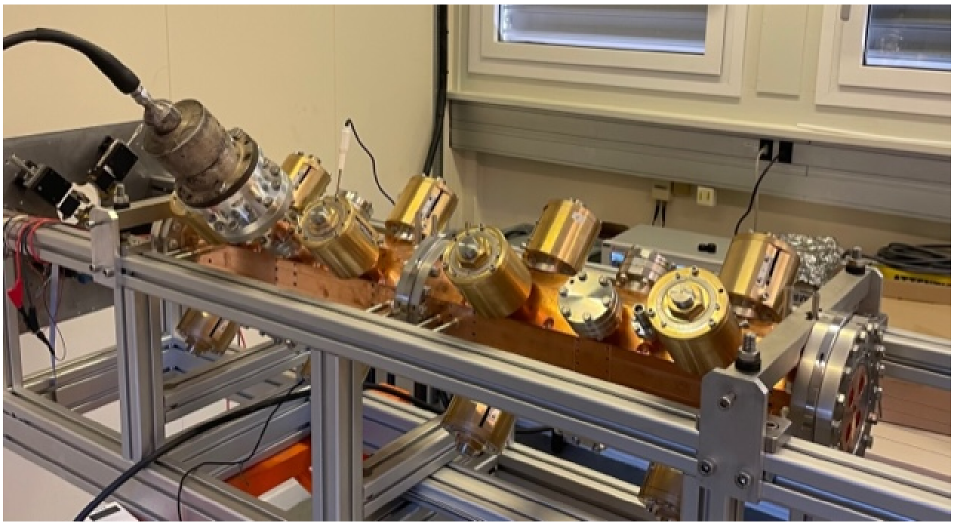

Figure 4.10. Full RFQ assembly model and photograph.

At the end of the tuning process, the tuners were cut to their final length and installed flange-to-flange with copper gaskets.

4.3.2 Tuning Algorithm

The ELISA-RFQ was tuned using the version of the tuning algorithm used for the tuning of PIXE-RFQ [4] (another RFQ accelerator operating at 750 MHz, which

constitutes a variant of the tuning algorithm developed for the medical accelerator HF-RFQ [8] [9].
The latter, based on the tuning scheme for the four-vane RFQ topology described in [12], permits the tuning of the field amplitude components through the collection of the first-order responses of the field, taken at the selected sampling points, linked to the individual movements of the tuners in a response matrix **R**.
The variant, which is an improved version applied also in the present case, can tune also the frequency, besides the field in the RFQ. In this way the response matrix describes the influence of each tuner on the three field amplitude components and on frequency at all longitudinal positions.
Referring to [8], the vector of quadrupole and dipole field components Q_i, D_i^S, D_i^T measured at the current tuner positions at the discrete sampling points $i = 1, ..., n$ is defined as

$$\vec{x}_{\text{cur}} = (Q_1...Q_n, D_1^S...D_n^S, D_1^T...D_n^T)^T \in R^{3n} \tag{4.7}$$

while, in analogy, the matching vector of the field components at the target tuner positions values is defined as

$$\vec{x}_{\text{trg}} = (Q_{\text{trg,1}}...Q_{\text{trg,n}}, D_{\text{trg,1}}{}^S...D_{\text{trg,n}}{}^S, D_{\text{trg,1}}{}^T...D_{\text{trg,n}}{}^T)^T \in R^{3n} \tag{4.8}$$

The current and target tuner positions, represented by t_j and $t_{\text{trg,j}}$ respectively with $j = 1, ..., m$ are gathered in the vector columns

$$\vec{t}_{\text{cur}} = (t_1...t_n) \in R^m, \vec{t}_{\text{trg}} = (t_{\text{trg,1}}...t_{\text{trg,m}}) \in R^m \tag{4.9}$$

By moving each tuner individually by some amount while maintaining the other ones in their nominal positions, the response matrix $\mathbf{R} = \delta\vec{x}_{\text{cur}}/\delta\vec{t}_{\text{cur}} \in R^{3n\times m}$ is obtained.
The response matrix **R** represents the Jacobian of the field amplitudes with respect to the tuner positions. Ideally an RFQ is characterized by having the quadrupole components equal to the unity and null dipole components at all sampling points. The aim of the tuning algorithm is to obtain, in the form of the response matrix outputs, the new tuner positions which correct the field distortions and frequency deviation present before the application of the algorithm.
Mathematically:

$$\vec{t}_{\text{trg}} = \vec{t}_{\text{cur}} + \mathbf{R}^\dagger \Delta\vec{x}, \tag{4.10}$$

where Δx is the difference between target and current field amplitudes and frequency and $\mathbf{R}^\dagger = (\mathbf{R}^T\mathbf{R})^{-1}\mathbf{R}$ denotes the Moore-Penrose inverse [15] of **R**, which in general is a nonsquare matrix. The inverse is computed using the method based on singular value decomposition (SVD) [15] proposed in Ref. [8] and used also in Ref. [4].

In the augmented version of the algorithm [4], the measured frequency is defined as a dimensionless quantity $\bar{f} = w_f f_{\text{trg}}$, through the introduction of a normalizing weight w_f, so that it can be combined with the dimensionless normalized measured field quantities and appended to the $\vec{x}_{\text{cur}}$ vector. In the same way, the target frequency value can be appended to the $\vec{x}_{\text{trg}}$ vector.
The normalizing weight can be modulated determining the contribution given by the frequency compared to the field amplitudes.
The response matrix $\mathbf{R}$ arising with the application of the augmented algorithm contains all dimensionless quantities and, differently from the original version, does not require to have all quadrupole components to be equal to unity. When the frequency is included a less strictly condition is applied to the quadrupole samples, that have to be set to a certain unknown value, close to the unity but not necessarily equal to it.
The resulting matrix is $\boldsymbol{R} \in R^{(3n+1)\times(m+1)}$ and, in order to obtain the new setting of tuner position, the system $\Delta\vec{x} = \mathbf{R}\Delta t$ must be solved. The solution vector $\Delta t \in R^{m+1}$ can be obtained if the pseudo-inverse (Moore-Penrose inverse) of the response matrix is computed, whose computation is proposed in Ref. [8] by means of a special method based on singular value decomposition (SVD).
With this method the response matrix is expressed as

$$\boldsymbol{R} = \boldsymbol{U}\boldsymbol{\Sigma}\boldsymbol{V}^T \tag{4.11}$$

$\mathbf{U} \in R^{N\times N}$ and $\mathbf{V} \in R^{M\times M}$, with $N = 3n+1$ and $M = m+1$, are orthonormal matrices. $\mathbf{\Sigma}$ is a rectangular diagonal matrix with the singular values of $\mathbf{R}$ in a descending order. The Moore-Penrose inverse of the response matrix is achieved by inverting each entry of $\mathbf{\Sigma}$ and by applying the transposition to the result. Due to the fact, for the smaller singular values of $\mathbf{R}$ possibly infinite quantities can be obtained after the operations of inversion and transposition, leading to invalid solutions (i.e. tuner adjustments lying outside the physical range), the method proposes to set to zero the largest entries of $\mathbf{\Sigma}^\dagger$. Having set to zero the k largest entries, with $k = 0, ..., (M-1)$, the matrices give M possibly useful solutions for the tuning goals, that are quadrupole field flatness and target operational frequency

$$\Delta\vec{t}_k = \boldsymbol{V}\boldsymbol{\Sigma}^\dagger_{\text{k}}\boldsymbol{U}^T\Delta\vec{x} \tag{4.12}$$

The eligible solutions are controlled with the computation of prediction of the corrected field and frequency using the initial response matrix:

$$\vec{\tilde{x}}_{\text{trg,k}} = \vec{x}_{\text{cur}} + \boldsymbol{R}\Delta\vec{t}_k \tag{4.13}$$

At the current tuning step, the set of tuner movements selected is the one to which the predictions fulfill the requirements better.

After the application of the tuner adjustments, RF measurements are carried out again and new current positions emerge. The implementation of the described algorithm is iterative and stops once the requirements are met with the desired accuracy.
In order to generate the response matrix **R**, its entries had to be determined. Each tuner was retracted by 3 mm, while all the others were kept at their nominal plus 11 mm position, and spectrum and bead-pull measurements were performed for each case.
Figure 4.11 shows a visual representation of the response matrix, reporting the sensitivity, in units of %/mm, of the Q (upper third of the plot), D^S (middle third) and D^T (lower third) component at one sampling point with respect to the tuner index, i.e. one tuner moved at a time. Referring to the quadrupole component of the plot, it can be seen that all four tuners at the same longitudinal position produce nearly the same effect on this component, whereas the ones located at the extremities of the RFQ produce stronger field tilts. Referring to the dipole components, it can be seen that two tuners positioned in opposite quadrants produce opposite effects on the correspondent dipole component, since each tuner influences heavily the dipole component relative to the quadrant in which the considered tuner is located, while the other component is almost not influenced at all.
Figure 4.11 reports, on the other hand , the frequency sensitivities, in kHz/mm, with respect to tuner movements at all sampling points. The frequency is affected by each tuner with approximately the same sensitivity of -55kHz/mm.

[]

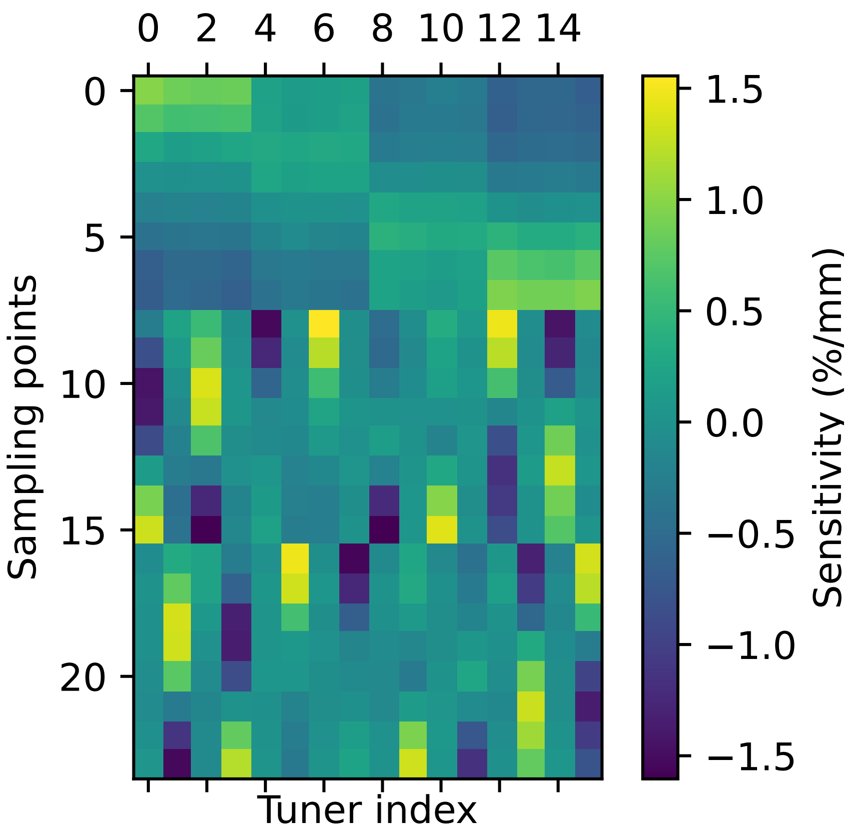

[]

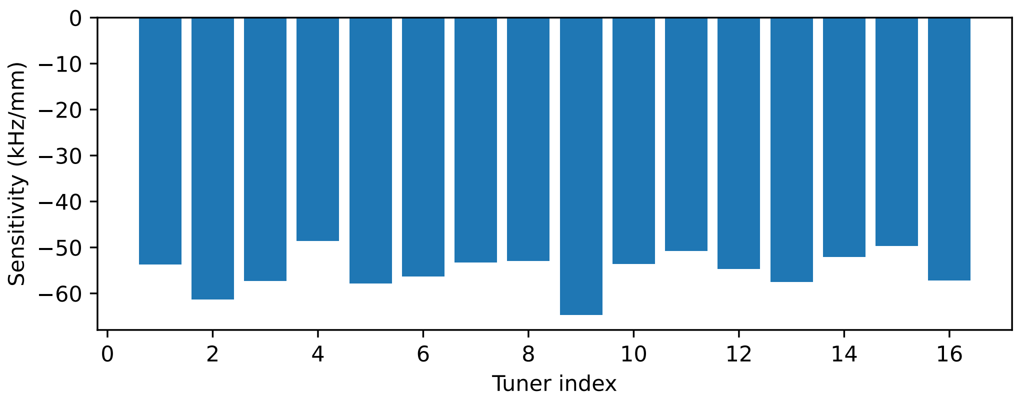

Figure 4.11. (a) Visual representation of $\mathbf{R}$ in which the entries represent Q, D^S, D^T sensitivities at one sampling point for each tuner movement. (b) Responses of operating mode frequency for each tuner movement.

4.3.3 Tuning Steps

The RFQ was tuned in four steps after the measurement of **R**: the first two were given by the algorithm whereas the last two were manual adjustments to fine-tune the frequency (all tuners moved by the same amount).
It was decided to move the tuners by half of the adjustments proposed by the algorithm at Step 1 and 2 of tuning since an overshooting had been observed. This likely originated in the non-linearity of the problem and that the quadrupole error was close to the measurement noise level already before tuning.
By applying the SVD to **R**, thus inverting the response matrix, for each tuning algorithm iteration, the construction of a set of M possible solutions for the corrective tuner movements Δt_{k} is derived 4.12. By using 4.13 the set of possible solutions lead to M predictions of the field profiles $\tilde{x}_{\mathrm{trg,k}}$ and, thus, field errors. The solutions are indexed by $k = 1, ..., M-1$. A plot of the field components errors as the index solution changes, related to the first tuning step, is reported in Figure 4.12. In this plot it can be seen that the solution with a lower k provide better corrections with respect to the solutions with an high index. The selection of the solution

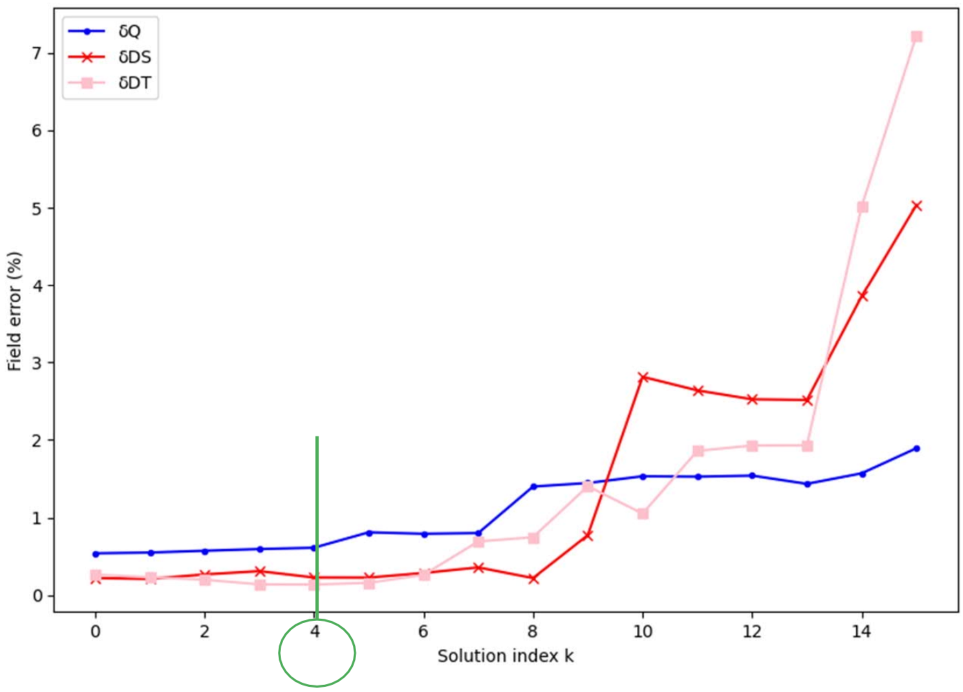

Figure 4.12. Field components errors, with respect to the target profiles, vs the k possible solutions, after applying the tuner adjustments given by the first tuning step. The index $k = 4$, highlighted in green, is the selected solution at this step.

to be implemented is dictated by the fact of obtaining significant improvements

while remaining within the range of possible and reasonable position adjustments of the tuners. Lower solution indexes correspond to wider movements of the tuners, so the selection of the first index does not strictly provide the best effect on the system. The way to proceed is by selecting the solution that represents the best compromise between improvements in terms of field and frequency tuning with small tuner adjustments given at each step and gradually reaching the tuning goals. In the case of the plot in Figure 4.12 the selected index is $k = 4$.
Below the partial tuning results, obtained for each step of the algorithm application, are reported in detail, highlighting the proposed tuner positions adjustments connected with the correspondent proposed and improved trend of the field components profiles and the frequency value. The algorithm improvements were verified with the measured data and the tuning procedure stopped when the difference between the measured trends and the target ones was well inside the error margins required and reported in 4.1.4.

Tuning Step 1

As mentioned previously, for the first tuning step, the selected solution is for $k = 4$ since it provided very small errors for all three field components, while proposing implementable tuner shifts.

Figure 4.13 shows a comparison of the field components errors, expressed in percentage, between the nominal case, meaning the original situation before the tuning process, the proposed one and the measured profiles after applying the tuner adjustments.
For the fields, a not negligible deviation between field prediction and measurement was observed, particularly for the D^T component, where an error of $-2.49\,\%$ is noticeable. Besides the measured TE_{210} read the value of 749.3456 MHz, which is lower than the target value and outside of the acceptable frequency error margin of $\pm 60\,\mathrm{kHz}$. As a consequence, a second tuning step was carried out, as reported in the following paragraph.

Tuning Step 2

For the tuning step 2 the chosen index solution was, once again, $k = 4$. As done for tuning step 1 the tables with numerical values of the tuner adjustments and the after measurement results are reported, as well as, the field errors plot showing the comparison between the measured profiles at step 1, the proposed ones at step 2 and the actual distributions collected after having carried out new measurements.

The results obtained for the field components fulfilled the requirements, listed in

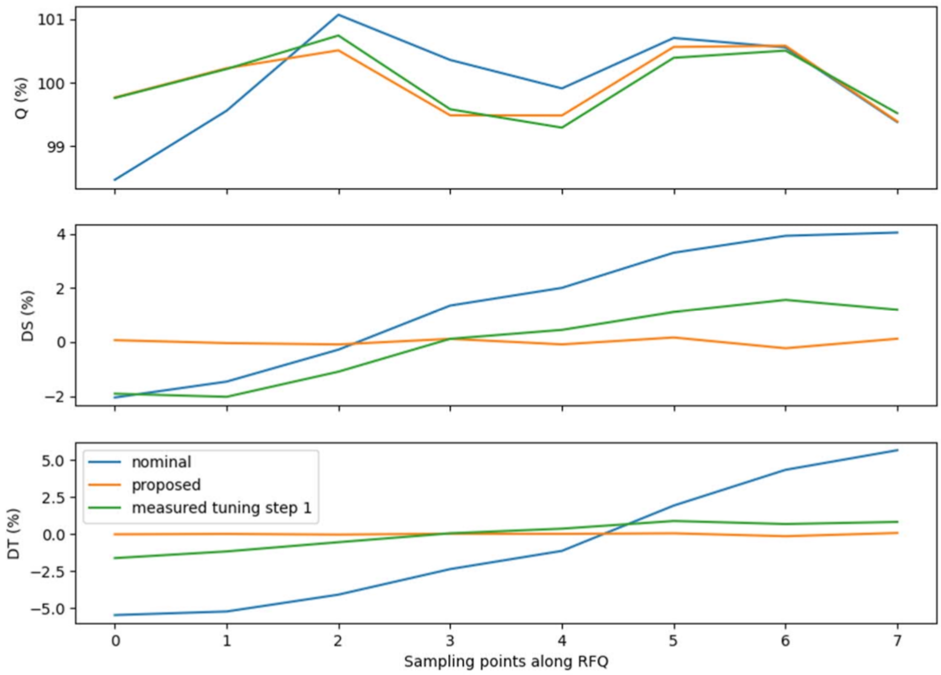

Figure 4.13. Comparison between nominal, proposed and after measurement situations in the errors of the field components for the tuning step 1.

section 4.1.4, meanwhile the measured TE_{210} frequency, reading 749.417 MHz, was closer to the target of 749.480 MHz but still not enough to be able to stop the tuning procedure at this point. In order to achieve a smaller error for the frequency, while maintaining the very good results in terms of field pattern and flatness, manual adjustments on the tuners were performed, as explained in the next section.

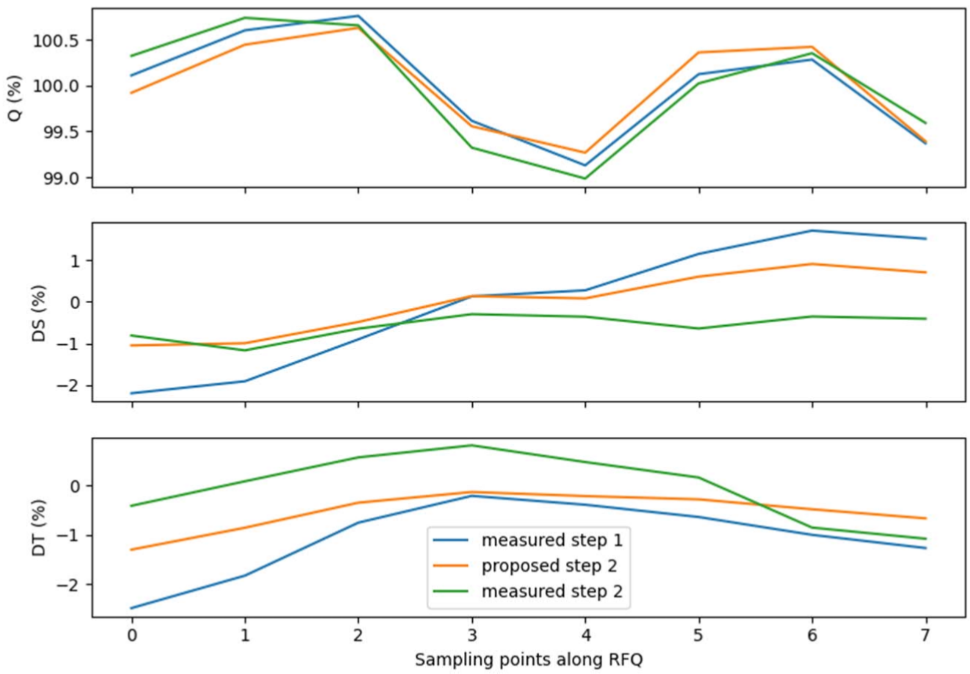

Figure 4.14. Comparison between nominal, proposed and after measurement situations in the errors of the field components for the tuning step 2.

Tuning Step 3 and 4

After tuning step 2 the frequency had to increase to meet the operational requirement, which imposes an error margin of ±60 kHz around the target value. To fine-tune the cavity manual adjustments on the position of the tuners were applied, moving all the tuners by the same amount.

At first all the tuners were retracted by 10 µm, measuring afterwards an higher operational frequency of 749.527 MHz. Since an over-shooting in the frequency value was observed, all the tuners were moved back again by 0.4 µm, reaching an excellent agreement between the subsequent measured value, amounting to 749.481 MHz and the target operational frequency.

In Figures 4.15 the values of the errors obtained at this step, the operational frequency and error profiles are reported.

% freq = 749481505.2219719 Hz	Column1	Column2	Column3
index	Q (%)	DS (%)	DT (%)
1	1.005	-0.0075	-0.0039
2	1.0077	-0.0067	0.0029
3	1.0065	-0.0007	0.0068
4	0.9945	0.0043	0.0079
5	0.9901	0.0029	0.0036
6	1.0007	0.0011	-0.0012
7	1.0018	0.0006	-0.0084
8	0.9937	-0.0039	-0.0119

Figure 4.15. Measured data after the implementation of the manual adjustements. The errors in the field components are reported as well as the measured TE_{210} operational frequency. All the values lie fairly within the acceptable error margins.

4.4 Tuning results

The errors in field components and frequencies are reported in Table 4.1 for each tuning step. After the second step, the errors in the field components fulfilled the requirements. As mentioned before, step 3 and 4 were performed in order to achieve the target tuning in terms of frequency.
Figure 4.17 shows the field components for each tuning iteration.
In Figure 4.18 a comparison between the field distributions along the RFQ before and after the tuning process is reported, which highlights the improvement obtained in terms of flatness and the achievement of the amplitude components values within the target margins.

Table 4.1. Errors in field components and frequency for tuning steps in chronological order.

Step	δQ (%)	δD^S (%)	δD^T (%)	Δf (kHz)
Initial	1.35	2.89	6.38	224.56
Step 1	0.87	1.91	2.49	134.31
Step 2	1.02	1.17	1.08	62.94
Step 3	—	—	—	-47.47
Step 4	0.99	0.75	1.19	-1.50

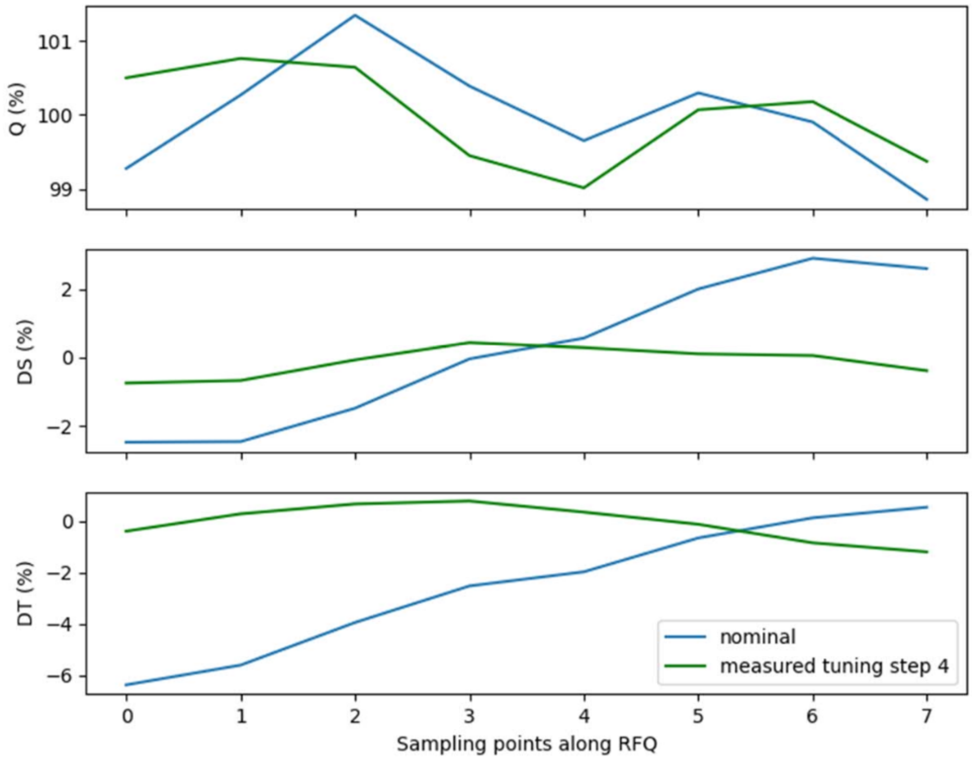

Figure 4.16. Comparison between the field errors situations before and after the implementation of the tuning procedure.

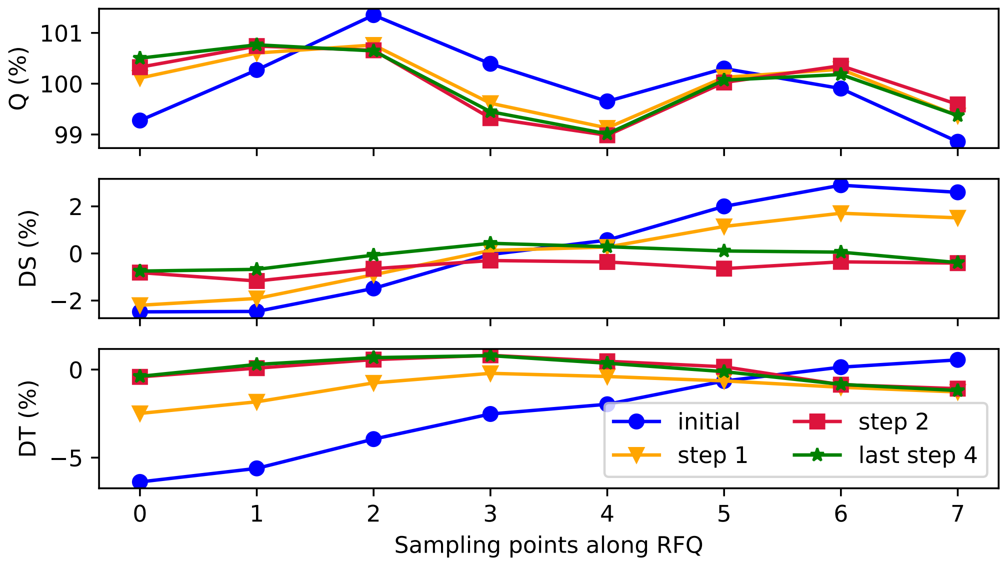

Figure 4.17. Measured field components for the initial tuner configurations and for each tuning step.

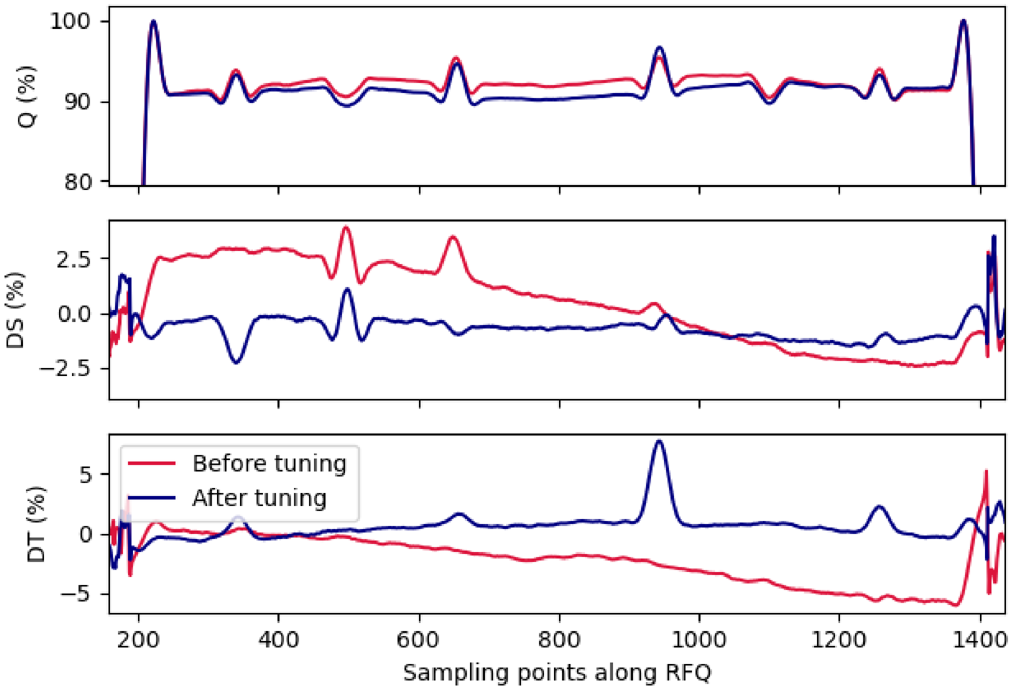

Figure 4.18. Profiles of the field components along the RFQ at all sampling points before and after the tuning procedure.

In Figure 4.18 a comparison between the field distributions along the RFQ before and after the tuning process is reported, which highlights the improvement obtained in terms of flatness and the achievement of the amplitude components values within the target margins.

4.5 Quality factor measurement

To validate the design of the present RFQ the quality factors were also measured. After tuning, the complex reflection coefficient Γ was measured in a bandwidth of 2 MHz around the operating frequency. Unloaded (Q_0), external (Q_{ex}), loaded (Q_ℓ) quality factors and the coupling coefficient (β_c) could be obtained by fitting an ideal circle to Γ following the method described in Refs. [16, 17, 18, 19]. In Table 4.2 measured quality factors and coupling coefficient are compared to the design values.

Table 4.2. Quality factors and coupling coefficient obtained through the circle-fitting method and their design values.

	Measured	Design	Rel. Error (%)
Q_0	6039	5995	0.7
Q_{ex}	4977	4796	3.8
Q_l	2728	2664	2.4
β_c	1.21	1.25	3.2

Chapter 5

Ceramic Input Power Coupler simulations and model

In this chapter the focus is put on the RF input power coupler featured in the RFQ linac object of the present thesis. It was decided to use a ceramic material for the RF window of the coaxial coupler structure, different from the PEEK material previously used, wanting to keep as much as possible the geometric design already existing. To meet RF performance constraints, in terms of reflected power, parametric simulations were carried out on the geometry of the previous design. At the end two new geometric configurations are proposed, which differ slightly from the original design, meeting the target reflection coefficient.

5.1 Input Power Coupler

The ELISA-RFQ features a single input power coupler which is mounted at the center of the second module of the cavity, in the longitudinal direction. It supplies the entire cavity with the power necessary to compensate the power loss inside the cavity walls. It follows that its design is based on the calculation of the RF power loss, which was determined by means of a semi-analitical approach. This technique sees the the RFQ split into multiple segments, as described in [3], and constitutes an efficient way through which it is possible to estimate the desired quantity accurately avoiding time-consuming 3D eigenmode simulations of the entire structure.
Its geometry and design parameters are the same of that of PIXE-RFQ [3] and it resembles a magnetic loop antenna which couples to the RFQ magnetic field and terminates to a coaxial waveguide.
For a nominal voltage of $V_0 = 35\,\mathrm{kV}$ the total power loss obtained is of 64.5 kW. By design, the coupler is 25 % over-coupled, presenting a coupling factor of $\beta_c = 1.25$, in order to have a margin accounting for deviations between simulated and the

measured unloaded quality factor Q_0. The coupler is mounted to a flange that can be rotated to provide the adjustment of the coupling according to the measured Q_0, such that critical coupling is achieved after assembly. Figure 5.1 reports the CAD models

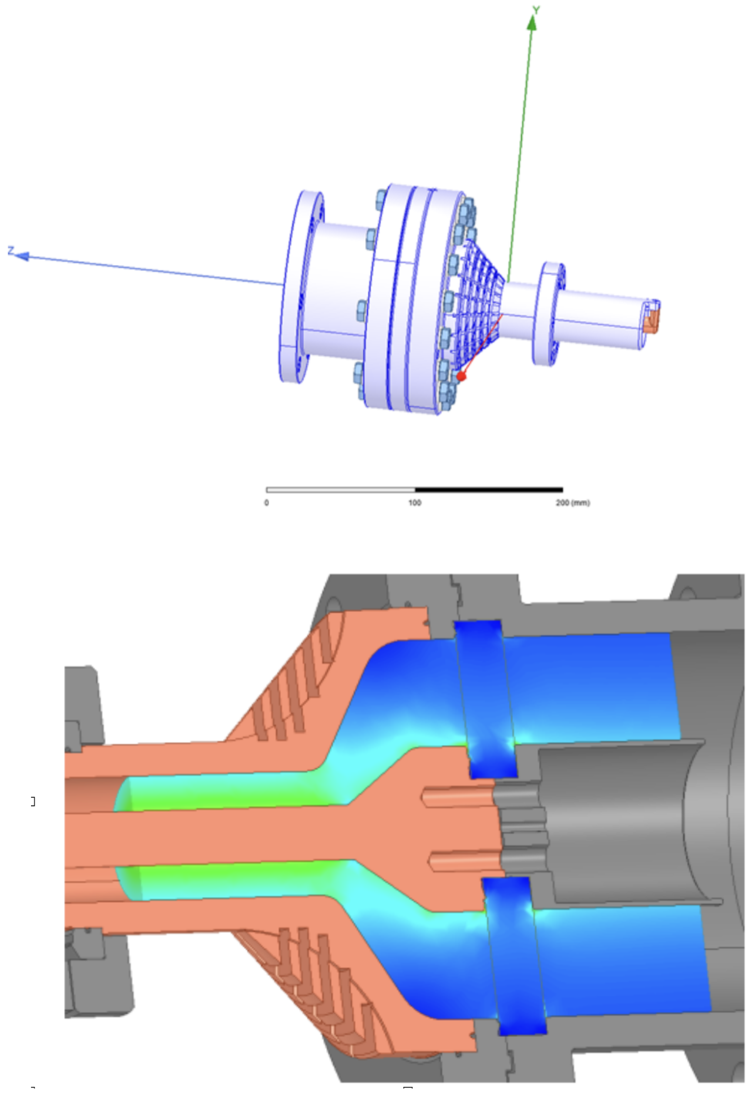

Figure 5.1. STEP model of the ELISA-RFQ assembly coupler. In the second picture is showed the cross-section of the coupler with the RF window used to separate the vacuum from the air domains- Courtesy of CERN SY Department

of the input power coupler in its full assembly and cross-section. In the PIXE-RFQ [3] the RF power is connected to the coupler by a taper and polyether ketone (PEEK) RF window. For ELISA-RFQ it was decided to perform an optimisation of the presented power coupler, based on the idea of substituting the PEEK window with a ceramic one.

In the following section 5.2 the RF simulations performed on the case of ceramic coupler are reported, which led to two different final proposed new geometric configurations.

5.2 RF simulations on the Ceramic Power Coupler

RF simulations were carried out using the electro-magnetic 3D modal simulator HFSS by Ansys on a slice of the section of the coupler containing the ceramic window and vacuum areas around it. The selected ceramic material is the aluminum oxide Al_2O_3, which is a chemical compound of aluminum and oxygen having the properties of electrical insulator with high thermal conductivity.
At first, the mechanical design from the preliminary drawings has been implemented with the only change in the window material. Figure 5.2 reports the the coupler half view, in which the slice useful for RF simulations is highlighted, and the slice model itself. By performing the RF simulations on the considered azimuthal slice of the coupler it was possible to perform fast simulations accounting for the entire coupler behaviour.
The slice can be represented as an ideal symmetric mono-modal structure, having the properties of reciprocity and low-losses, that can be studied by applying an analytical approach using a cascade of two-port networks. For mechanical reasons it was decided to consider as a constraint the thickness of the RF ceramic window, which was set to be equal to 5 mm. Also, at first, the electrical permittivity of the ceramic material was set to the value 9. With no other change in geometrical values, the two reflection coefficients at the input and output ports of the structure, S_{11} and S_{22} respectively, were simulated as function of frequency, around the ideal resonance frequency of 750 MHz. The obtained plot is reported in Figure 5.3. It is desirable to achieve a reflection coefficient below the value of -40 dB. It can be seen that the two reflection coefficients have almost the same value of -32.7 dB, but it is not sufficient to reach the target.
In order to achieve a better RF performance, in terms of reflected power, geometrical modifications in the ceramic window area have been analyzed.
Two types of geometrical changes were considered and parametric studies were carried out. In particular the two parameters considered modifiable were the gapped area length and the inner conductor radius in the gapped area around the RF window. In Figure **??** it is reported the mechanical sketch regarding the section of the coupler object of the study, where the modifiable length of the area around the window is in blue and the inner radius of the same area of the coaxial structure is in orange.

Along with the geometric variations a parametric study of the ceramic window electric permittivity ϵ_r was useful to take into account its tolerance and find the

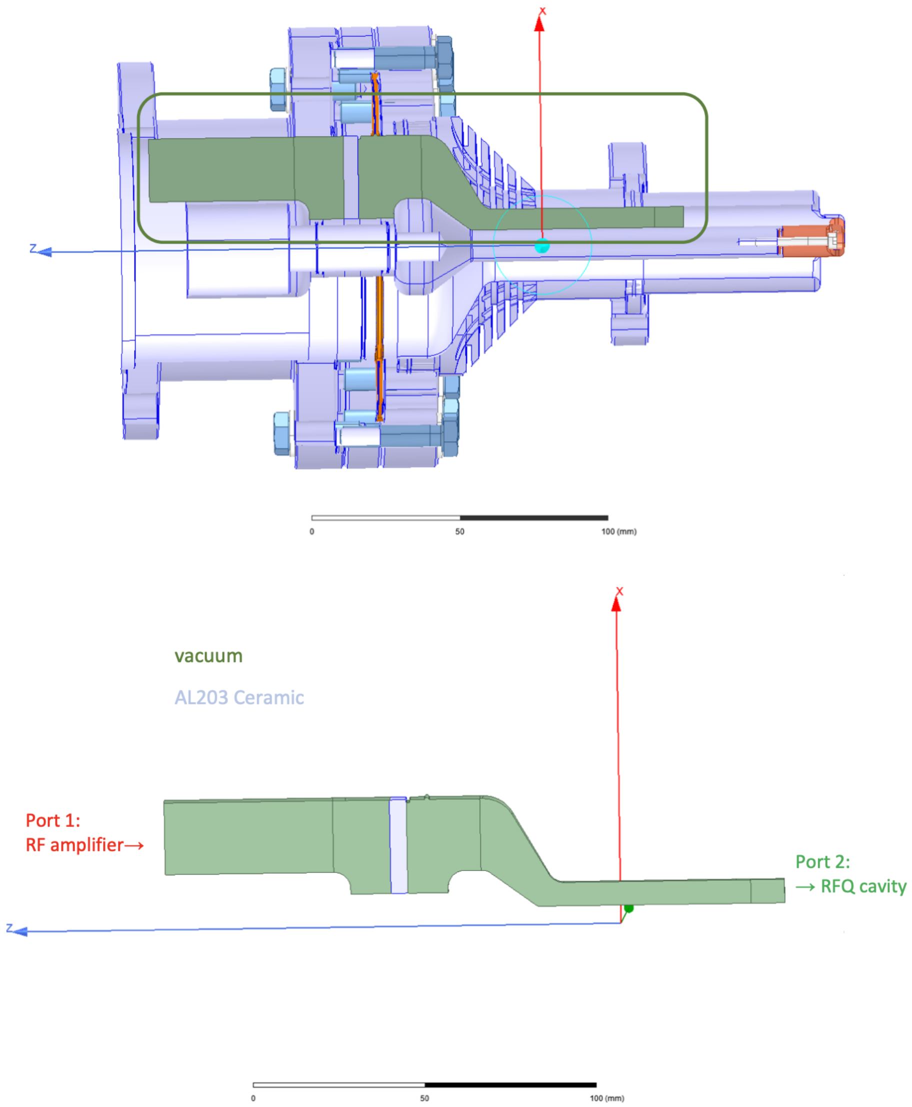

Figure 5.2. Coupler half-view and the extracted model used for RF simulations. The green part stands for the vacuum areas around the Al_2O_3 ceramic window, in silver.

trade-off between all the considered parameters. The resulting plots of the parametric simulations are reported in Figure 5.5. By decreasing linearly the ceramic electrical permittivity, starting from the ideal value of 9.8 (i.e. 99 % Al_3O_3 ceramic), less variation of the geometric value is needed.

From this information two design proposals were derived:

- Gap length=13.5 mm, Inner radius=10 mm (nominal value), $\epsilon_r = 9.6$;
- Inner radius=9.6 mm, Gap length=12 mm (nominal value), $\epsilon_r = 9.6$;

The two proposals are mutually exclusive and they presents a variation in one of the

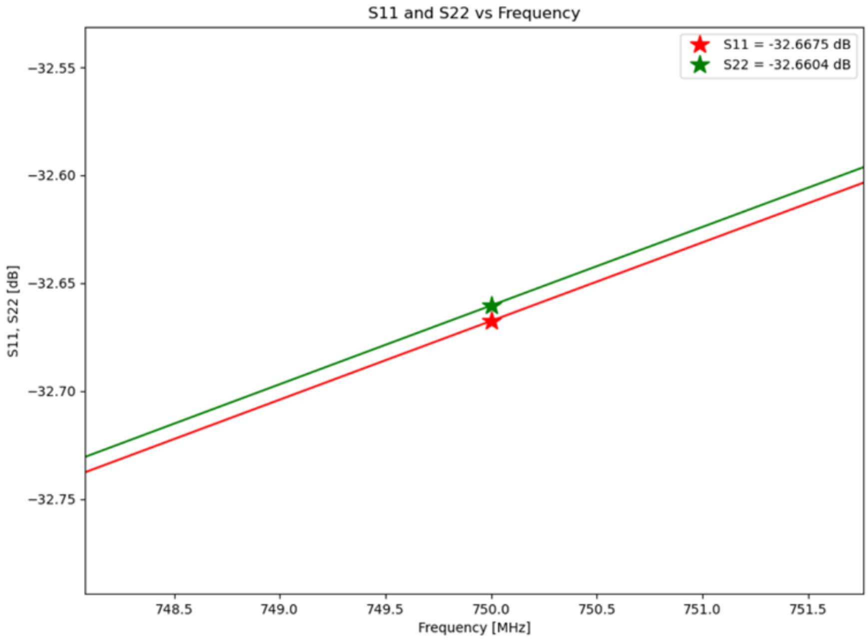

Figure 5.3. S_{11} and S_{22} vs. frequency plot of the coupler implementation with no geometrical changes with respect to the previous design, excluding the change in the window material and thickness.

two geometric parameters each, while the other one can be kept at its original value (nominal value). The value of the electrical permittivity of 9.6 was selected since it is the one that shows the best tolerance taking into account the ceramic quality. Figure 5.6 reports the plotted reflection coefficients as a function of frequency, in a range around the operation frequency, of both the proposals. In the first case $S_{11} = -46.98\,\mathrm{dB}$, whilst in the second case $S_{11} = -46.64\,\mathrm{dB}$ making both the new configurations suitable from an RF point of view.

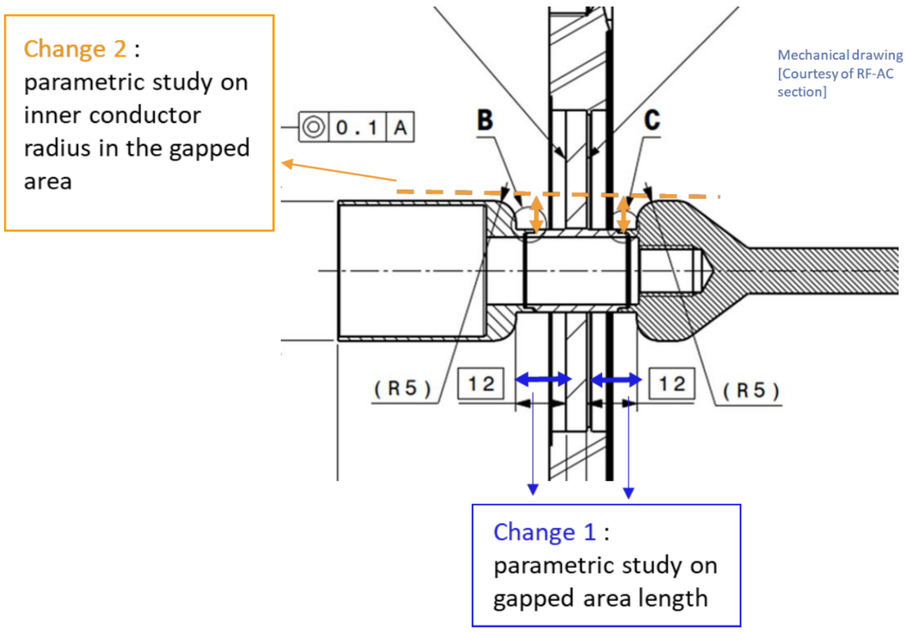

Figure 5.4. Mechanical drawing of the coupler half-view with highlighted geometric figures object of the parametric simulations. Courtesy of CERN RF-AC sections.

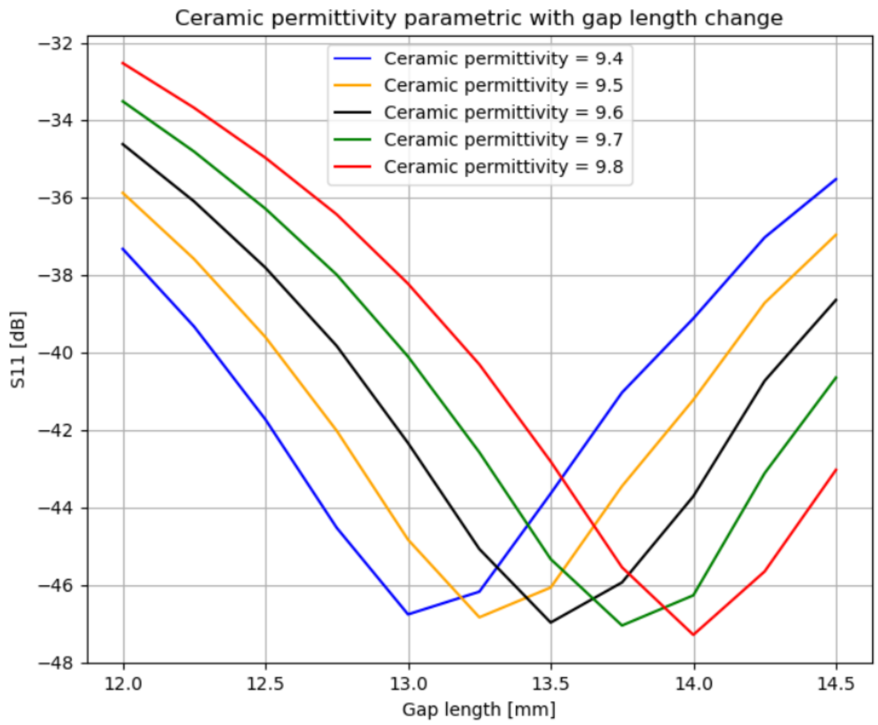

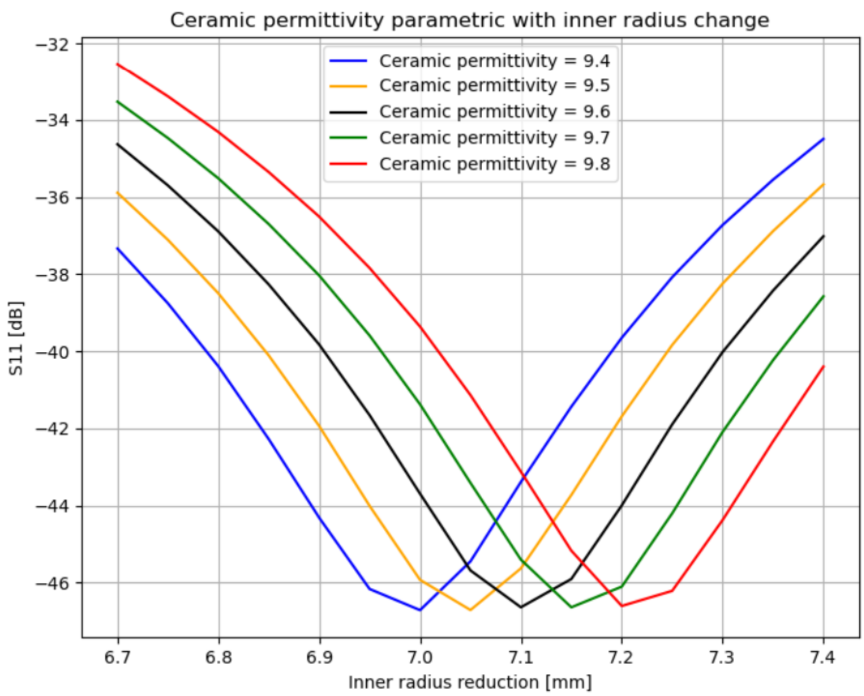

Figure 5.5. Parametric plots showing the input reflection coefficient S_{11} as a function of the gapped area length and inner radius reduction of the gapped area around the RF ceramic window, respectively, for different values of the ceramic electrical permittivity.

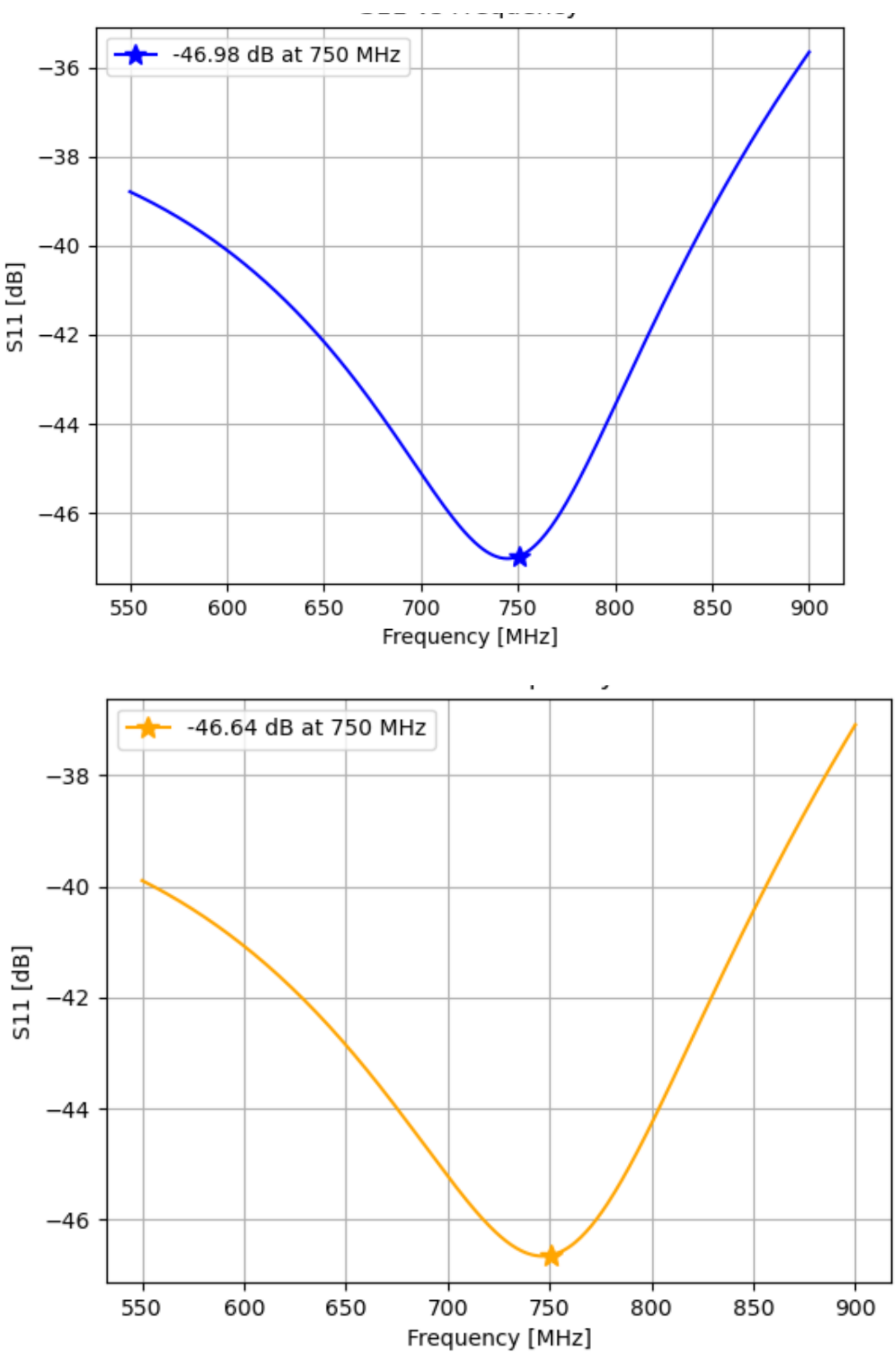

Figure 5.6. S_{11} versus frequency for the two proposed configurations of the ceramic input power coupler.

Chapter 6

General Conclusion

The present thesis covers the characterization and tuning of a compact radio-frequency quadrupole linear accelerators (RFQ) operating at 750 MHz and simulations regarding its RF auxiliaries. After providing the reader with the foundations forming the basis of the thesis in Chapter 2, the main thesis body is composed of two main parts: Chapter 4 covers the low-power RF measurements and tuning of the ELISA-RFQ, a one-meter long proton accelerator for ion beam analysis. Chapter 5 is dedicated to the electro-magnetic simulations of single input power coupler of the ELISA-RFQ, with the aim to provide geometric configurations which would work appropriately, from an RF point of view, considering a change in the material in one of the crucial parts of the coupler structure, the RF window.
The main point of the present work is represented by the low-power RF measurements and tuning of the 750 MHz ELISA-RFQ. Bead-pull measurements on individual mechanical modules have shown the high manufacturing quality of the RFQ. Also the RFQ electromagnetic field, decomposed into a quadrupole and two dipole contributions, was measured by means of bead-pull measurements. Machining imperfections and misalignments cause longitudinal and transverse field tilts that were compensated with the help of movable piston tuners. The necessary tuner adjustments were calculated by means of an augmented version of an algorithm. The new variant allows for tuning both field and frequency at the same time. The remaining field and frequency errors have been successfully corrected using an iterative tuning procedure, with final values well within target ranges. Moreover, excellent agreement was observed in quality factors and coupling.

Bibliography

[1] M. Vretenar, E. Montesinos, M. Timmins, M. Garlasch‘e, A. Grudiev, S. Mathot, B. Koubek, V. Dimov, A. M. Lombardi, and D. Mazur, High-frequency compact RFQs for medical and industrial applications, in 28th Linear Accelerator Conference (LINAC2016), East Lansing, MI, USA (JACoW, Geneva, Switzerland, 2016) pp. 704–709.

[2] A. Lombardi, M. Vretenar, S. Mathot, and A. Grudiev, High frequency compact low-energy linear accelerator design, US Patent 10,051,721 (2018), current assignee: CERN (European Organization for Nuclear Research).

[3] H. W. Pommerenke, A. Bilton, A. Grudiev, A. M. Lombardi, S. Mathot, E. Montesinos, M. Timmins, M. Vretenar, and U. van Rienen, RF design of a high-frequency RFQ linac for PIXE analysis, in 29th Linear Accelerator Conference (LINAC2018), Beijing, China (JACoW, Geneva, Switzerland, 2018) pp. 822–825.

[4] H. W. Pommerenke, V. Bencini, A. Grudiev, A. M. Lombardi, S. Mathot, E. Montesinos, M. Timmins, U. van Rienen, and M. Vretenar, rf design studies on the 750 MHz radio frequency quadrupole linac for proton-induced x-ray emission analysis, Physical Review Accelerators and Beams 22, 10.1103/physrevaccelbeams.22.052003 (2019).

[5] S. Mathot, G. Anelli, S. Atieh, A. Bilton, B. Bulat, T. Callamand, S. Calvo, G. Favre, J.-M. Geisser, A. Gerardin, A. Grudiev, A. Lombardi, E. Montesinos, F. Motschmann, H. W. Pommerenke, P. Richerot, K. Scibor, M. Timmins, M. Vretenar, F. Taccetti, F. Benetti, L. Castelli, M. Chiari, C. Czelusniak, S. Falciano, M. Fedi, P. A. Mand‘o, M. Manetti, C. Matacotta, E. Previtali, C. Ruberto, V. Virgili, and L. Giuntini, The CERN PIXE-RFQ, a transportable proton accelerator for thE machina project, Nuclear Instruments and Methods in Physics Research Section B: Beam Interactions with Materials and Atoms 459, 153 (2019).

[6] . M. Lombardi, E. Montesinos, M. Timmins, M. Garlasch‘e, A. Grudiev, S. Mathot, V. Dimov, S. Myers, and M. Vretenar, Beam dynamics in a

high-frequency RFQ, in 6th International Particle Accelerator Conference (IPAC2015), Richmond, VA, USA (JACoW, Geneva, Switzerland, 2015) pp. 2408–2412.

[7] M. Vretenar, A. Dallocchio, V. A. Dimov, M. Garlasch'e, A. Grudiev, A. M. Lombardi, S. Mathot, E. Montesinos, and M. Timmins, A compact high-frequency RFQ for medical applications, in 27th Linear Accelerator Conference (LINAC2014), Geneva, Switzerland (JACoW, Geneva, Switzerland, 2014) pp. 935–938.

[8] B. Koubek, A. Grudiev, and M. Timmins, rf measurements and tuning of the 750 MHz radio frequency quadrupole, Physical Review Accelerators and Beams 20, 10.1103/physrevaccelbeams.20.080102 (2017).

[9] B. Koubek, A. Grudiev, and M. Timmins, RF measurements and tuning of the 750 MHz HF-RFQ, Tech. Rep. CERN-ACC-NOTE-2017-0006 (CERN, Geneva, Switzerland, 2017).

[10] V. A. Dimov, M. Caldara, A. Degiovanni, L. S. Esposito, D. A. Fink, M. Giunta, A. Jeff, A. Valloni, A. M. Lombardi, S. J. Mathot, and M. Vretenar, Beam commissioning of the 750 MHz proton RFQ for the LIGHT prototype, in 9th International Particle Accelerator Conference (IPAC2018), Vancouver, BC, Canada (JACoW, Geneva, Switzerland, 2018) pp. 658–660.

[11] P. Balleyguier, 3D design of the IPHI RFQ cavity, in 20th Linear Accelerator Conference (LINAC2000), Monterey, 13 CA, USA (SLAC, Menlo Park, CA, USA, 2000).

[12] T. P. Wangler, RF Linear Accelerators, 2nd ed. (John Wiley Sons, 2008).

[13] B. Koubek, Y. Cuvet, A. Grudiev, C. Rossi, and M. Timmins, Tuning of the CERN 750 MHz RFQ for medical applications, in 28th Linear Accelerator Conference (LINAC2016), East Lansing, MI, USA (JACoW, Geneva, Switzerland, 2016) pp. 763–766.

[14] H. W. Pommerenke, U. van Rienen and A. Grudiev, rf measurements and tuning of the 1-meter-long 750 MHz radio-frequency quadrupole for artwork analysis , arXiv:2011.09920v1 [physics.acc-ph].

[15] I. N. Bronshtein, K. A. Semendyayev, G. Musiol, and H. M¨uhlig, Handbook of Mathematics (Springer Berlin Heidelberg, 2015).

[16] W. Altar, Q circles-a means of analysis of resonant microwave systems, Proceedings of the IRE 35, 478 (194).

[17] D. Kajfez, Linear fractional curve fitting for measurement of high q factors, IEEE Transactions on Microwave Theory and Techniques 42, 1149 (1994).

[18] . D. Kajfez, Random and systematic uncertainties of reflection-type Q-factor measurement with network analyz.er, IEEE Transactions on Microwave Theory and Techniques 51, 512 (2003).

[19] V. A. Goryashko, L. Han, H. Nicander, S. Teerikoski,K. Gajewski, L. Hermansson, R. S. Kern, R. Ruber, and D. Dancila, High-precision measurements of the quality factor of superconducting cavities at the FREIA laboratory, in 17th International Conference on RF Superconductivity (SRF2015) (JACoW, Geneva, Switzerland,2015) pp. 810–813.

[20] R. E. Collin. Foundations for Microwave Engineering. 2nd ed. McGraw-Hill, 1992. ISBN: 0070118116. DOI: 10.1109/9780470544662.

[21] D. M. Pozar, Microwave Engineering; 3rd ed. Hoboken, NJ: Wiley, 2005. [Online]. Available: https://cds.cern.ch/record/882338

[22] I. M. Kapchinsky and V. A. Teplyakov. "A linear ion accelerator with spa- tially uniform hard focusing". In: Prib. Tekh. Eksp. USSR 4 (1970), pp. 19– 22.

[23] A. Schempp. "Radio-frequency quadrupole linacs". In: CAS - CERN Ac- celerator School: Radio Frequency Engineering, Seeheim, Germany. Available as CERN-2005-003. CERN, Geneva, Switzerland, 2000, pp. 305–314. DOI: 10.5170/CERN-2005-003.305.

[24] T. P. Wangler. "Lumped-circuit model of four-vane RFQ resonator". In: 1984 Linear Accelerator Conference (LINAC84), Seeheim, Germany. Gesellschaft für Schwerionenforschung m.b.H., Darmstadt, Germany, 1984, pp. 332–334.

[25] R. P. Feynman, R. B. Leighton, and M. Sands. The Feynman Lectures on Physics: New Millenium Edition. 3 vols. Originally published 1963–1965. Basic Books, 2010. ISBN: 9780465023820.

[26] L. G. Hector and H. L. Schultz. "The dielectric constant of air at radiofrequencies". In: Physics 7.4 (1936), pp. 133–136. DOI: 10.1063/1.1745374.

[27] M. Santo Zarnik and D. Belavic. "An experimental and numerical study of the humidity effect on the stability of a capacitive ceramic pressure sen- sor". In: Radioengineering 21.1 (2012), pp. 201–206.

[28] A. L. Buck. "New equations for computing vapor pressure and enhance- ment factor". In: Journal of Applied Meteorology 20.12 (1981), pp. 1527–1532.

[29] Buck Research Instruments LLC. Model CR-1A hygrometer with autofill, operating manual. Ed. by A. L. Buck. 2012. URL: http : / / www . hygrometers . com / wp - content / uploads / CR - 1A - users - manual-2009-12.pdf (visited on 06/29/2020).

[30] A. Savitzky and M. J. E. Golay. "Smoothing and differentiation of data by simplified least squares procedures." In: Analytical Chemistry 36.8 (1964), pp. 1627–1639. DOI: 10.1021/ac60214a047.

[31] H. Wiedemann. Particle Accelerator Physics. Graduate Texts in Physics. Springer International Publishing, 2015. ISBN: 9783319183176. DOI: 10.1007/978-3-540-49045-6.

[32] S. Mathot et al. "The CERN PIXE-RFQ, a transportable proton accelerator for the machina project". In: Nuclear Instruments and Methods in Physics Research Section B: Beam Interactions with Materials and Atoms 459 (2019), pp. 153–157. ISSN: 0168-583X. DOI: 10.1016/j.nimb.2019.08.025.

[33] L. Giuntini et al. "MACHINA: movable accelerator for cultural heritage in-situ non-destructive analysis". In: 16th International Conference on Nu- clear Microprobe Technology and Applications (ICNMTA2018), Guilford, Sur- rey, England. 2018.

[34] J. C. Maxwell. A Treatise on Electricity and Magnetism. Clarendon Press, 1873. ISBN: 9780511709333. DOI: 10.1017/cbo9780511709333.